THESIS FOR DEGREE OF DOCTOR OF PHILOSOPHY IN CHEMISTRY

Integrated Biomechanical, Electronic and Topographic Characterization of Titanium Dental Implants

by

Johanna Löberg

UNIVERSITY OF GOTHENBURG

Department of Chemistry
University of Gothenburg
Gothenburg, Sweden, 2011

Department of Chemistry
University of Gothenburg

Correspondence:
Johanna Löberg
University of Gothenburg
Department of Chemistry
412 96 Göteborg
Sweden

or

Astra Tech AB
P.O. Box 14
431 21 Mölndal
Sweden

Email: Johanna.Loberg@chem.gu.se
Johanna.Loberg@astratech.com

ISBN 978-91-628-7872-6
E-publication: http://hdl.handle.net/2077/25023

Printed by Chalmers Reproservice

Cover illustration: Scanning Electron Microscope images of titanium samples with (from right to left) turned surface (TS), blasted surface (CB) and blasted surface treated with sequential oxalic acid and diluted hydrofluoric acid (CB+AT1). The graph shows the ability of the different surface topographies to induce retention strength with bone calculated by the Local Biomechanical model.

ABSTRACT

Titanium dental implants are medical devices used to restore the function entailed with the loss of one or several teeth. To obtain successful function over long periods, the dental implants must be sufficiently anchored in the bone to withstand the forces induced by for example chewing. Two important factors for obtaining high anchorage strength are *i)* the chemical composition of the material and *ii)* the implant design at all length scales. Topographical features on different length scales induce for example nucleation sites for collagen and minerals, cell attachment and biomechanical stimulation necessary to prevent bone resorption and eventually to gain bone.

The design of nucleation sites at the titanium surface to stimulate bone growth is at the heart of the project presented in this thesis. The aim of the work is to in detail characterize the implant surface and design chemically as well as topographically modified surfaces by complementary experimental studies including electrochemical characterization and biomechanical models. The present thesis is based on three main topics of importance for dental implants: *i)* Surface topography measured with scanning electron microscopy and atomic force microscopy, *ii)* Biomechanical modelling and *iii)* Electronic properties of the surface oxide film investigated using impedance spectroscopy and cyclic voltammetry.

Theoretical finite element studies have shown that the micro-topography of a surface can be designed to induce optimal biomechanical stimulation for bone formation. However, currently used topographical characterization methods for describing dental implant surfaces are insufficient to characterize the topography in the required detail to design such surfaces. In the present thesis, a method to investigate and describe the micro- to nanosized surface topographies is presented. In this method, complementary analysis techniques are used in combination with overlapping analysis areas and data filtering in order to obtain information from surface features in a wide range of length scales. Theoretical models have also been developed with the aim of evaluating the ability of micro- and nanoscaled surface features to induce retention strength with bone. By combining the characterization method and the theoretical models, an integrated characterization method is presented which can be used to design biomechanically optimized implant surfaces with suitable surface topography.

Various modification techniques are used to alter the surface topography and as a secondary effect, the electronic properties of the oxide film will be altered. The effects on the biological response induced by changes in topography and electronic properties separately are therefore difficult to distinguish. The present thesis includes a study where the electronic properties of the surface oxide film were deliberately changed without significant changes in surface topography. The results show that the electronic properties of the oxide film have larger effects on the cellular attachment and apatite nucleation than a small change in topography and that a less insulating oxide film is preferable for titanium dental implants.

The knowledge obtained from the biomechanical models and the electronic investigation was used to design well-characterized nanostructured surfaces created by coating titanium discs with titanium dioxide nanoparticles of different morphology and size. The bioactivity of the coated samples was evaluated by apatite formation and the results show that the coated samples induce earlier apatite nucleation and form thicker apatite layers than the uncoated reference.

The results obtained and presented in this thesis suggest that dental implants should have roughness at different length scales in combination with formation of a thin defect rich oxide. Such an implant is still to be designed and tested under realistic conditions.

Keywords: Surface roughness parameters, 3D-SEM, AFM, Interfacial shear strength, Impedance spectroscopy, Cyclic voltammetry, SBF, MG-63, TiO_2 nanoparticles.

PREFACE

This thesis is based on the work presented in the following papers. The papers will be referred to by their Roman numerals in the text.

I. Semi-conducting properties of titanium dioxide surfaces on titanium implants.
Petersson, I., Löberg, J., Fredriksson, A., Ahlberg, E.
Biomaterials 30 (2009) 4471-4479

II. Characterisation of dental implants. I: Critical assessment of surface roughness parameters.
Löberg, J., Mattisson, I., Hansson, S., Ahlberg, E.
The Open Biomaterials Journal 2 (2010) 18-35

III. Characterisation of dental implants. II: Local biomechanical model
Hansson, S., Löberg, J., Mattisson, I., Ahlberg, E.
The Open Biomaterials Journal 2 (2010) 36-52

IV. Global biomechanical model for dental implants
Hansson, S., Löberg, J., Mattisson, I., Ahlberg, E.
Journal of Biomechanics 44 (2011) 1059-1065

V. Integrated Biomechanical and Topographical Surface Characterization (IBTSC): Implant surfaces with hierarchic structures
Löberg, J., Mattisson, I., Ahlberg, E.
Submitted 2010-12

VI. Electronic properties of anodized TiO_2 electrodes and the effect on bioactivity.
Löberg, J., Gretzer, C., Mattisson, I., Ahlberg, E.
Submitted 2011-05

VII. Electronic properties of TiO_2 nanoparticle films and the effect on bioactivity.
Löberg, J., Perez Holmberg, J., Mattisson, I., Arvidsson, A., Ahlberg, E.
Manuscript

Statement of contribution:

Paper I, provided topographical information and SEM images and participated in the discussion of the results. Papers II, VI and VII, all experimental work and analysis except the synthesis and characterization of the nanoparticles and the cell study. Contributed in writing the papers. Paper III, all experimental work and calculations, contributed in writing the paper. Paper IV, participated in the discussions and contributed in writing the paper. Paper V, all experimental work and analysis and writing most of the paper.

TABLE OF CONTENTS

1. INTRODUCTION

Dental implants commonly used today are made of titanium or titanium alloys with a screw shaped design and a rough surface. This implant design has shown excellent performance with long-term stability and is the result of many years of development [1-3]. Current developments of dental implants are mainly related to shortening the healing time and improving the aesthetics. It is also a wish to use dental implants in bone with lower quality than possible today. The challenge is to design an implant with these new characteristics without affecting the long-term stability already achieved. One of the aspects very much in focus is the biomechanics. For example, a roughened surface introduces biomechanical forces that stimulate and enhance the cellular response [4-6]. Mechanical stimulation on varied length scales are also crucial to prevent bone resorption and to preserve or even regain bone [7-9].

The part of the implant surface that is in contact with the body fluid is the surface oxide film which properties are highly important for the biocompatibility of the implant material [10,11]. Interactions at the oxide/solution interface only slightly contribute to the force associated with primary anchorage of the implant with the bone but can be of decisive importance indirectly by providing a good platform for the new bone formation. Although various physical and chemical properties of implant surfaces are generally considered decisive factors for the biocompatibility of materials, the mechanism of new bone formation is still not known on a molecular level. However, improved biological response for titanium implants has been shown by altering the chemical properties of the surface [12-15] as well as by introducing nanostructures or nanosized surface features [16-18].

As more knowledge is gained regarding the properties of the implant surface that have effects on the biological response, the possibility to design implants with specific properties increases. However, further developments are necessary since for example, the techniques used to characterize implant surfaces today give insufficiently detailed description of the topography. In addition, focus has mostly been on topographical and chemical aspects while

other properties of the material, such as the electronic conduction of the surface oxide [19-21], may be equally important for the biological response.

The objective of the present work was to gain better understanding of the electronic and topographic properties of titanium implants and how these properties influence, at different time and length scales, the practical outcome in dental implant applications. By combining electrochemical and topographical techniques with biomechanical theories, this thesis adds new insight to implant research and technology. The thesis is based on the seven appended papers, summarized in three main chapters: Chapter 3 – Biomechanics and implant topography – comprises an integrated characterization method where the importance of evaluating the surface roughness at variable length scales are considered as well as its effects on retention strength with bone, Papers II, III, IV and V. In Chapter 4 – Modification of the titanium oxide film – oxide films with different electronic properties are topographically and electrochemically characterized and the effects on cell response and apatite formation evaluated, Papers I and VI. Finally, Chapter 5 – Nanostructures – includes a study where titanium dioxide nanoparticles were spin-coated onto substrates to create electrochemically as well as topographically modified surfaces, which were evaluated with the respect to apatite formation, Paper VII.

2. EXPERIMENTAL

2.1. Sample preparation

Commercially pure titanium discs (Grade IV) with a turned surface were used in all experiments. The discs were cleaned and degreased before altering the topography and/or chemistry of the surfaces according to different modification techniques described below.

Physical and chemical treatment

Physical modification was performed by blasting the turned samples with TiO_2 particles of two sizes creating fine- (FB) and coarse- (CB) blasted surfaces with different surface roughness. Chemical treatments were performed by using oxalic acid and/or dilute hydrofluoric acid (HF), which influences the topography of the surface and chemical composition as well as electric properties of the surface oxide film, Papers I, II, III and V. The FB sample represents the surface of the commercial TiOblast™ implant (Astra Tech AB) and the CB surface treated with diluted HF acid (CB+HF) represents the surface of the commercial OsseoSpeed™ implant (Astra Tech AB).

Anodized samples

In Paper VI, the turned titanium discs were modified by galvanostatic anodization to 20.0 V using current densities of 2.4, 4.8 or 11.9 $mVcm^{-2}$ (geometric areas). The anodization was performed in 0.5 M H_2SO_4 and both potential and current were recorded. After reaching 20.0 V, the potential was kept constant at 20.0 V for 5 minutes in order to create a stable oxide.

Spin-coated samples

In Paper VII, titanium dioxide (TiO_2) nanoparticles of three sizes, 8, 22 and 30 nm were spin-coated onto disc shaped samples. Particles of 8 and 22 nm were synthesized by hydrolysis from a $TiCl_4$ solution and consisted predominately of anatase [22]. The 30 nm particles were commercially available titanium dioxide particles (Degussa P25) extensively washed prior to

use in order to remove organic impurities from the particle surfaces. The spin-coated samples are hereafter referred to as coated.

2.2. Electrochemical analysis

2.2.1 Instrumentation

Potentiostat and frequency analyzer

The electrochemical experiments performed in Paper I were carried out using an EG&G Princeton Applied Research potentiostat/galvanostat model 273A together with a Schlumberger frequency response analyzer SI1255 for the impedance measurements. In Papers VI and VII, a Gamry Reference 600™ Potentiostat/Galvanostat/ZRA was used. The general instrumental set-up is shown in Figure 2-1.

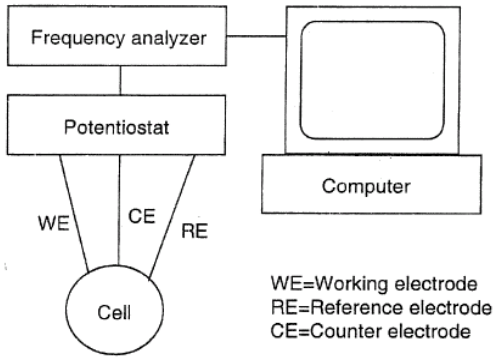

Figure 2-1. *Experimental setup for electrochemical measurements.*

Cells

The electrochemical experiments in Paper I were performed in a conventional three electrode cell consisting of a 150 ml titration vessel and a lid with the ability to use a rotating disc electrode, Figure 2-2a. For the electrochemical experiments performed in Papers VI and VII, electrochemical experiments were carried out in the setup shown in Figure 2-2b. The sample is placed at the bottom of the cell with the modified surface towards the electrolyte. A large Pt counter electrode is concentrically placed around the sample to assure optimal current distribution and the reference electrode (Ag/AgCl, sat KCl) is place in the middle of the cell. During the electrochemical experiments, a three-electrode system was used with the exception of the anodization where only two electrodes were employed.

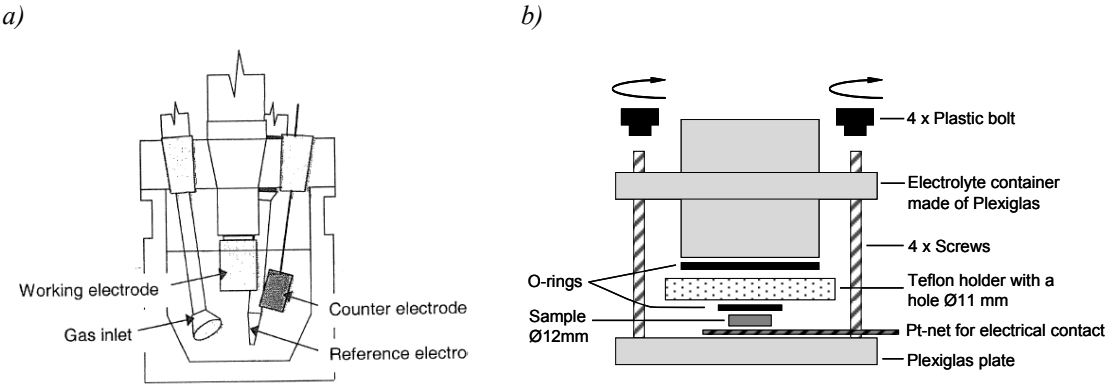

Figure 2-2. *Cell setup for electrochemical experiments performed in a) Paper I, b) Papers VI and VII.*

Electrodes

Disc shaped samples, with only the modified surface exposed to the electrolyte, were used as working electrodes. Large platinum net was used as counter electrode for the electrochemical and anodization experiments. All potentials were referred to a double junction Ag/AgCl electrode (E = 197 mV vs. SHE) with the inner compartment filled with saturated KCl solution and the outer junction filled with the actual electrolyte.

2.2.2 Electrochemical techniques

Cyclic Voltammetry

Cyclic voltammetry (CV) is an electrochemical analysis technique where the potential is varied linearly with time and the responding current is measured. Figure 2-3 a) shows a typical CV waveform and b) the cyclic voltammogram for a turned titanium surface. The Ti(IV)/Ti(III) redox couple in the surface oxide film is readily observed.

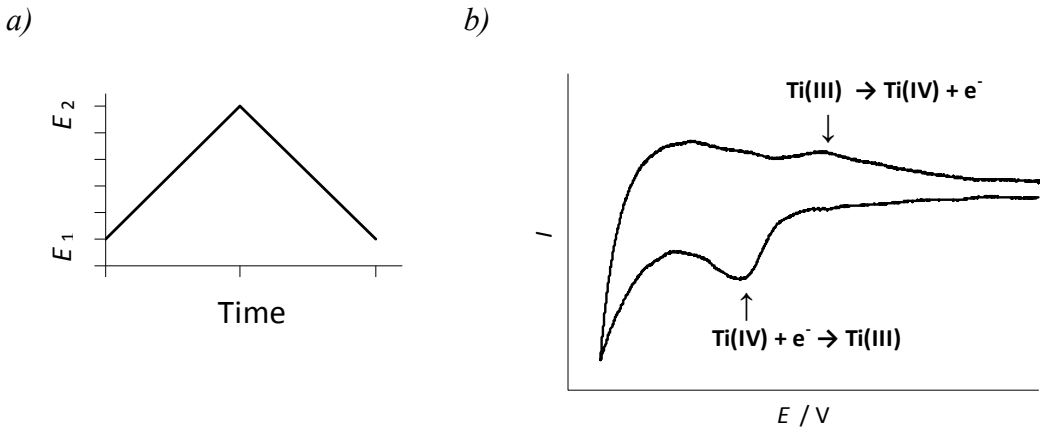

Figure 2-3. *a) Potential-time profile for cyclic voltammetry (CV). b) A CV scan for a turned titanium surface. Scan rate of 50mVs^{-1}.*

Except for the electrolyte and electrode material, variable parameters are for example scan rate and sweep range. The technique can be used to obtain information regarding electrochemical processes taking place at the electrode surface such as adsorption/desorption of species, reversibility and kinetics of the electrochemical reactions taking place.

In the present work, CV was used to study the change in peak potential for the Ti(IV)/Ti(III) redox couple and density of states (DOS) between differently modified samples, Papers VI and VII. CV was performed in deoxygenated 0.1 M KOH solution with a sweep rate of 50 mVs^{-1}.

Electrochemical Impedance Spectroscopy (EIS)

In EIS a small alternating potential or current is applied to the cell. This signal induces a perturbation of steady state and the impedance response is measured in a wide frequency range. The impedance can be divided into a real (*Z'*) and an imaginary (*Z''*) part where the phase shift as well as the magnitude give information regarding the resistive and capacitive behaviour of the specimen. The impedance response is analyzed by fitting the data to equivalent circuits or physical models [23]. EIS is useful for experiments requiring a complete analysis of complicated processes involving both surface and solution reactions.

In the present work, EIS was used to investigate the impedance behaviour of modified turned and blasted titanium discs, Papers I, VI and VII. Two different equivalent circuits were used to fit the obtained data and these are shown in Figure 2-4.

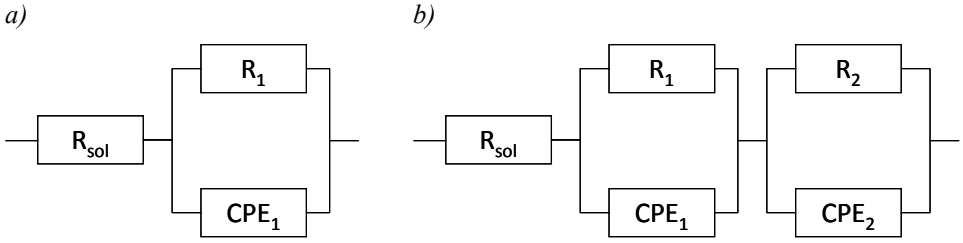

Figure 2-4. *Equivalent circuits used in the evaluation of impedance data. R_{sol} is the solution resistance while R_1 and R_2 correspond to resistances of the oxide film. CPE_1 and CPE_2 are the constant phase elements of the oxide film.*

The solution resistance is coupled in series with one or two parallel circuits involving the resistance and capacitance of the oxide layer. Instead of a pure capacitance, constant phase elements (CPE) are used to account for the frequency dependent capacitance often observed. Depending on the degree of frequency dispersion (α), the physical meaning of the CPE element differs. For α = 0 and 1 pure resistive and capacitive behaviour is observed,

respectively. Intermediate values of α can be understood as distribution of properties due to heterogeneous surfaces, inhomogeneous films or mass transfer, for example. EIS measurements were performed at open circuit potential (OCP) in deoxygenated 0.5 M H_2SO_4. The frequency was scanned between 100 kHz-10 mHz with an amplitude of 10 mVrms and 9 points/decay. EIS measurements were also performed at potentials ranging from +1 to -0.5 V in order to measure the electronic properties of the surface oxide utilizing the Mott-Schottky relation, Equation 2-1, Papers I and VII. In paper VI, the Mott-Schottky analysis was done by measuring the impedance response at 100 Hz between +2 and 0 V with a sweep rate of 10 mVs^{-1}.

$$C^{-2} = \frac{2}{e\varepsilon\varepsilon_0 N_D A^2}\left(E - E_{fb} - \frac{kT}{e}\right) \qquad \text{Equation 2-1}$$

2.3. Surface morphology and topographic characterization

2.3.1 Techniques

Two different techniques were used for studying the surface morphology and topographical characteristics: 3D-Scanning Electron Microscopy (3D-SEM) and Atomic Force Microscopy (AFM).

Atomic Force Microscopy (AFM)

AFM is a scanning probe technique where a sharp tip mounted on a cantilever is scanned over the surface with constant velocity and pressure [24]. Tapping Mode is a non-contact AFM mode where the probe is oscillating above the surface and the van der Waals forces of the surface affects the oscillation, which is translated into height information. Analysis can be performed at atmospheric pressure and high-resolution data up to a few Ångström can be achieved [25]. However, limitations due to sensitivity of vibrations and maximum vertical range can reduce the application range [24,26]. AMF was used for topographical characterization of the turned and modified surfaces in Papers II, III and V as well as for anodized and coated samples in Papers VI and VII.

Scanning Electron Microscopy (SEM)

SEM is a microscopy technique where an electron beam is scanned over the sample surface. The electron beam induces a larger depth of focus than a regular light beam and images at

very high resolution can be recorded [27]. The high energetic electron beam induces elastic scattering of the sample electrons, which gives information both from the surface as well as from the underlying bulk material. The analyzed volume is called the *interaction volume* and its size depends highly on the energy of the incoming beam. A reduction of the beam energy reduces the interaction volume and the depth of focus. SEM analysis can be utilized on all electric conducting samples which can withstand high pressures [27]. To obtain topographical information from SEM images, 3D-models have to be created. This is achieved by taking two images at the same spot, but with a separating angle, and then put these two images together. It is highly important that the centre of both images is at the same spot otherwise a distorted 3D-model is obtained which gives unreliable data [28].

In Papers VI and VII, SEM was used to study the morphology of samples before and after cell cultivation and/or SBF immersion. In Papers II and III, 3D-SEM was used for topographical characterization of both turned and blasted samples.

MeX®

MeX® [29] is a software from Alicona Imaging which transforms 3D-SEM images into a dense dataset that can be used to investigate the topography of surfaces. Depending on the resolution and magnification of the 3D-SEM images, topographical information on macro to sub-micro levels can be obtained [29]. The MeX® software supports import of AFM ASCII data files which thereby enables reliable comparison of calculated surface roughness parameters from different techniques. The MeX® software offers the possibility to perform 3D-area analysis where a range of 3D surface roughness parameters is calculated. By using the area analysis together with applying a Gaussian filter of different sizes in the MeX® software, topographical information on different levels can be obtained. In Papers II, III, and V, care was taken to systematically measure at the same spot on the surface during the processing procedure, for example going from a turned surface to a blasted and chemically modified final sample. By using three or four 3D-SEM magnifications and three AFM scan sizes, topographic information on the scale from 250 μm to 150 nm was obtained. Detailed information regarding the MeX® analysis can be found in Paper II and in [30].

2.3.2 Surface roughness parameters

In 1994, Dong, Sullivan and Stout [31-33] presented a set of mathematically defined parameters, which in detail can describe the topography of all kind of engineered surfaces in

3D. The set of 3D parameters are divided into groups describing different properties of the surface topography such as amplitude, spatial and volume. In Paper II, parameters from these groups were, together with parameters often used to describe surface roughness of implants, evaluated with respect to dental implant applications. This analysis identified four parameters of specific importance, which are recommended to be used for characterizing surfaces of dental implants i.e. S_a *(Average height of the analyzed area)*, S_{dr} *(Developed interfacial area ratio)*, S_{dq} *(Root-mean-square of surface slope)* and V_{vc} *(Void volume in core zone)*, Paper II and [30]. The mathematic descriptions of these parameters are shown in Table 2-1.

Table 2-1. *Surface roughness parameters.*

S_a	Average height of the analyzed area (μm) $S_a = \frac{1}{l_x l_y} \int_0^{l_x} \int_0^{l_y} \lvert \eta(x, y) \rvert \, dx \, dy$
S_{dr}	Developed interfacial area ratio (%) $S_{dr} = \frac{\int_0^{l_y} \int_0^{l_x} \sqrt{1 + \left(\frac{\partial \eta(x, y)}{\partial x} \right)^2 + \left(\frac{\partial \eta(x, y)}{\partial y} \right)^2} \, dx dy - l_x l_y}{l_x l_y} \times 100\%$
S_{dq}	Root-mean-square of the slope of the surface $S_{dq} = \sqrt{\frac{1}{l_x l_y} \int_0^{l_y} \int_0^{l_x} \left[\left(\frac{\partial \eta(x, y)}{\partial x} \right)^2 + \left(\frac{\partial \eta(x, y)}{\partial y} \right)^2 \right] dx \, dy}$
V_{vc}	Core void volume of topographic surface (ml/m^2)

l_x and l_y are the side lengths of the sampling area.
η is the height distance from the reference plane [31-33].

2.4. Material characterization

Energy-dispersive X-ray spectroscopy (EDX)

EDX analysis is performed within the SEM instrumentation. When the incoming electron beam interacts with the sample, this can cause emission of X-ray photons due to the excitation and relaxation of sample atoms. Since the emitted X-ray photons are characteristic to each element, EDX is used for both qualitative and quantitative elemental analysis [27]. However, no information regarding chemical compounds can be obtained, only the overall element composition. EDX was used in Paper VI and VII to detect the amount of apatite formed after simulated body fluid (SBF) immersion.

X-ray diffraction (XRD)

XRD is an analysis technique where an X-ray beam is projected onto the sample. If the material is crystalline, the incoming beam interacts with the atoms in the 3D-crystal structure which then emits radiation specific to the lattice parameters. The constructive interference between the initial X-ray beam and the emitted radiation from the atom creates characteristic diffraction patterns, which can be used to identify chemical composition, crystallographic structure and phase of the sample. XRD analysis can be used on a wide range of samples such as powders, thin films, solids etc. The incoming X-ray beam is highly energetic and can, depending on material, penetrate the surface of the sample. By using gracing-angle XRD (GI-XRD) the incident angle of the incoming beam can be varied and information from smaller volumes close to the surface obtained.

XRD was used to evaluate the crystalline phase of the anodized and coated samples before and after immersion in simulated body fluid (SBF) in Papers VI and VII.

X-ray Photoelectron Spectroscopy (XPS)

XPS method is a technique, which uses a more focused X-ray beam with lower energy than the X-ray beam used in XRD. Due to the low energy level, the outermost surface (~6nm) of the specimen is analyzed and information about composition, chemical state, electronic structure and geometric structure of sample surface can be obtained [34].

XPS was used to investigate the composition of the anodized and coated samples in Paper VI and VII.

2.5. Cell and Simulated Body Fluid (SBF) studies

In order to investigate the biological response of the surfaces in Papers VI and VII, two *in vitro* methods were used; cellular response and apatite formation in simulated body fluid.

Cell study

A cell study was performed to investigate the interaction between cells and the anodized surfaces in Paper VI using human osteoblast-like cell line MG-63. Osteoblasts are the early "bone forming" cells, which together with another important cell type, the osteoclasts, are crucial in the bone remodelling process continuously takes place in our bones. The cells were harvested after 3, 7 and 14 days of culture. Cell adhesion and morphology after 36h were investigated by SEM. The number of cells present on the different surfaces after the different

times was evaluated by measuring the amount of DNA. The promotion of osteoblast activity and inhibition of osteoclast activity were evaluated by measuring the extracellular Prostaglandin E_2 (PGE_2) and Osteoprotegerin (OPG) levels. To evaluate the early mineralization and differentiation of osteoblasts, the Alkaline phosphate (ALP) levels in the cells as well as in the supernatant were measured.

Simulated Body Fluid (SBF)

SBF is a solution that contains ion concentrations similar to human blood plasma [35,36], which is supersaturated with respect to apatite. Hydroxyapatite is the hydroxylated form of apatite, $Ca_5(PO_4)_3(OH)$, and is an important mineral in our bones [36,37].

In Papers VI and VII, anodized and coated surfaces were immersed in revised SBF solution [35], for 12 h, 72 h, and 1 week at 37.0 °C. The samples were mounted up-side down to avoid gravitational precipitation on the surfaces. The amount and morphology of the formed apatite were evaluated by using EDX, SEM and XRD.

3. BIOMECHANICS AND IMPLANT TOPOGRAPHY

Bones are constructed at levels ranging from macro to nanoscale in hierarchical order. The structure, composition and organization of these levels are optimized with respect to each other in order to create the remarkable mechanical properties of our bones [38,39]. Bone properties such as structure and mass are affected by the mechanical forces which it is subjected to [9]. This connection is for example utilized in the design of the neck portion of a dental implant where a smooth surface has been replaced by a neck comprising of retention elements such as threads to allow the surrounding bone to be mechanically stimulated [7,40,41]. The bone adaption to an implant can be studied by structural and compositional analysis of the tissue close to the implant surface [38]. Studies have shown that the bone-implant interface has reduced levels of collagen and/or minerals as compared to the unaffected bone [42-44] and therefore has lower mechanical strength [44,45]. The size of this interface zone of reduced mechanical strength can be decreased by increasing the roughness of the implant topography. This gives an increased surface area and mechanical stimulation of the bone tissue on different levels [6,46-49].

The early Brånemark implants had a smooth surface topography and although the screw-shaped design of the titanium implants gave increased bone anchorage compared to a cylindrical implant, fibrous tissue was often formed at the implant surface [50]. By using implants with micro-roughened surfaces, this fibrous encapsulation was prevented and improved bone-to-implant contact, removal torque (RTQ), pull-out and push-out forces were obtained as compared to implants with a smooth titanium surface [3,51-54]. Surface features at the micro-scale have also been shown to improve the affinity to adhere osteoblasts and increase the activity for cells adhered to roughened surfaces compared to smooth [55-59]. Due to the above mentioned reasons commercial implants today typically have surface roughness at different length scales comprising micro-, sub-micro- and nanoscaled structures. In order to characterize such surfaces in detail and further improve the descriptions of key elements for implant topography, new methods for characterizing and interpretation are continuously required.

3.1. Characterization of implant topographies

The texture of a surface is generally divided into three categories; form, waviness and roughness depending on the wavelength of texture components [60]. The form and waviness are related to the design and to the natural variation induced by the manufacturing technique to create the raw material. To remove the form and waviness from dental implant surfaces, a Gaussian filter with a size of 50×50 μm is recommended where topographical information from surface features larger than 50 μm is removed [26]. However, using a filter of one size is not sufficient to describe the topography of dental implants which consists of surface features in a wide range of scales. For example, the contribution to surface roughness from nanosized features might be masked by surface features of larger sizes that influences the roughness much more. Fractal analysis, wavelet filtering [61-65] and Fast-Fourier-Transform [66,67] are methods which have been used to analyze surface roughness induced by surface features of variable length-scales. Another technique was utilized in Paper II where topographical information from surface features ranging from 250 μm to 150 nm was obtained by using *i)* complementary analysis techniques (AFM and 3D-SEM), *ii)* overlapping SEM magnifications and AFM scan sizes, *iii)* a Gaussian filter with a band-gap of 100 and varied size. Figure 3-1 illustrates SEM and AFM images taken at different magnifications and scan sizes of a turned surface treated with diluted hydrofluoric acid (TS+HF). From these images, it is clearly shown that overlapping magnifications and scan sizes are necessary to visualize the different structure levels of the surface.

3.1.1 Using surface roughness parameters to describe topography

Surface topography is traditionally described by mathematically defined surface roughness parameters where parameters describing the roughness of 2D-profiles have been utilized since the 1960's. However, with the development of new analysis techniques, parameters describing 3D-surfaces are now possible to obtain. In 1994 Dong, Stout and Sullivan suggested a set of 3D-surface roughness parameters to characterize all kinds of mechanically made surfaces [31-33,60]. These parameters describe different properties of the topography such as amplitude, bearing, texture etc. To standardize the characterization of surfaces in 3D an ISO standard has recently been published, ISO 25178.

Surfaces roughness parameters are generally scale-dependent which means that the parameter values can change depending on measurement scale and sampling interval [67].

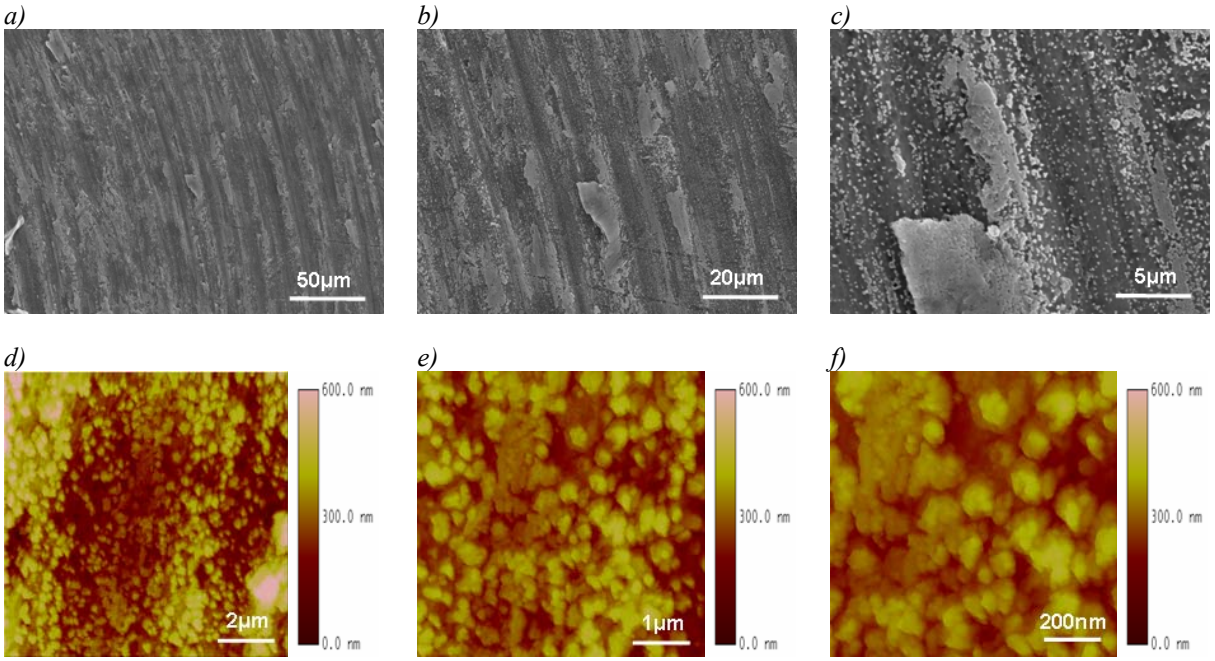

Figure 3-1. *Overlapping SEM magnifications and AFM scan sizes on the same point of a turned surface treated with diluted HF acid (TS+HF). a-c) show SEM images taken at ×500 (248×186 µm), ×1200 (103×78 µm) and ×5000 (25×19 µm) magnification, respectively. d-f) show AFM at scan sizes of 10×10, 5×5 and 3×3 µm, respectively. SEM settings:, 30kV, WD = 10 mm (ESEM XL30). AFM settings: 0.8 Hz, 512 scan lines (Multimode SPM IIIa).*

Because of this, it is important to clearly state the technique, filter size and settings used when topographical information is published and discussed [26,66,68]. Wennerberg *et al.* [26] proposed a set of guidelines for how to characterize the topography of dental implants. The authors suggested that screw-shaped implants should be analyzed at the thread top, valley and flank and that at least one height, spatial and hybrid parameter should be included when describing the surface topography. In Paper II, the parameters proposed by Dong, Stout and Sullivan [31-33] and Wennerberg *et al.* [26] were evaluated with respect to usefulness in dental implant applications. A total amount of 13 surface roughness parameters was evaluated, including their length-scale dependence. This was done by analyzing the surface topography of former and today commercially available dental implants (TiOblast™ and OsseoSpeed™, Astra Tech AB) and intermediate surfaces. The length-scale dependence was obtained by using complementary analysis techniques, overlapping magnifications and a Gaussian filter of varied sizes, in detail described in Section 2.3 and Paper II. This analysis was further extended to include newly designed implant surfaces consisting of surface features in a wider size range, Paper V and [69]. Of the initially 13 parameters, four parameters were considered especially valuable when describing the topography of dental implant surfaces. The parameters were: *i) Average height of the analysed area* (S_a), *ii)*

Developed interfacial area ratio (S_{dr}), *iii) Root-mean-square of surface slope* (S_{dq}) and *iv) Void volume in core zone* (V_{vc}). S_a is a height parameter which is commonly used to describe surfaces of dental implants. The S_{dq} and S_{dr} are hybrid parameters and describe the slope and the surface enlargement compared to a smooth surface, respectively [31,32]. The volume parameter V_{vc} is defined from the bearing property of the topography and gives information regarding the amount of fluid that the surface can hold, e.g. in the form of blood which is important during the healing process [39,70]. The mathematical definitions of these parameters are shown in Table 2-1. Using these four parameters it is possible to separate between topographically similar surfaces provided that the length-scale dependence is evaluated, Paper II and V. An example of this is given in Figure 3-2 where SEM images of blasted surfaces treated with a) oxalic acid (CB+AT2), b) oxalic acid and diluted HF acid sequentially (CB+AT1) and c) diluted HF acid (CB+HF) are shown. In Figure 3-2d, the length-scale dependence of the S_a parameter can be seen when measured on these three surfaces using 3D-SEM. The values farthest to the right are obtained when a Gaussian filter of 50×50 μm is applied which is the recommended filter size when analyzing dental implant surfaces [26]. At this length-scale, no difference in surface roughness can be observed although the surfaces clearly have different morphology, Figure 3-2a-c. However, when applying filters of smaller sizes (towards lower log filter size values in Figure 3-2d), separation between the treated surfaces can be obtained. From the graph in Figure 3-2d it can be determined that the oxalic acid treatment induces additional hierarchical levels [69] which gives increased S_a values as compared to blasted surfaces treated with HF only (CB+HF), Paper V. The sequential treatment of the oxalic acid treated surfaces with diluted HF acid induced yet another hierarchical level on top of the former structures [69]. In addition, this fine structure separates the (CB+AT1) and (CB+AT2) surfaces at the lowest filter sizes for the S_a parameter, Figure 3-2d, Paper V. This interpretation is not possible without the visual information obtained from the SEM images. Without an image of the surface, a correct interpretation of the surface parameter values is almost impossible and this should not be made since topographically different surfaces can exhibit the same parameter values [71]. Because of this, it is also important that complementary parameters are used in order to give a correct description of the surface topography.

3.1.2 Theoretical models to evaluate the bone-implant interaction

The performance of design and topography of dental implants is evaluated by *in vivo* studies

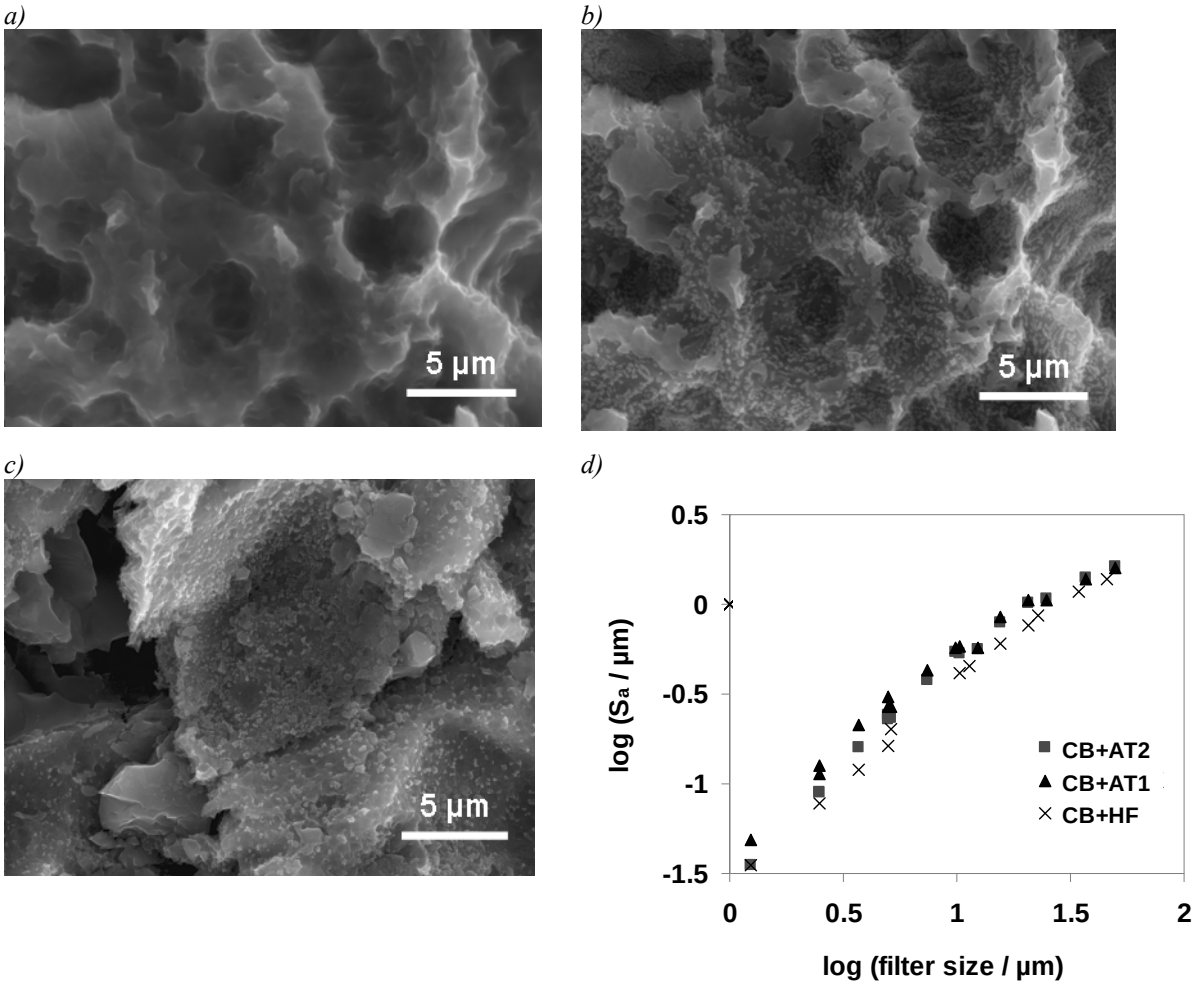

Figure 3-2. *a-c) show SEM images of CB+AT2, CB+AT1 and CB+HF surfaces, respectively at the lowest SEM magnification, ×5000 (25×19 µm) used in the 3D-SEM topography evaluation. d) shows the length-scale dependence for the S_a parameter measured at these surfaces. The points farthest to the right show the value obtained if a Gaussian filter of 50×50 µm is applied. SEM settings; 30kV, WD = 10mm (ESEM XL30).*

where the interaction between a surgically placed implant and the bone is measured after a certain healing time. This interaction is measured by the forces required to either break the bonds between the bone and the implant by a pull, push or torque motion. The latter is called Removal Torque (RTQ) and measured forces are proportional to the interfacial shear strength between implant and bone. The S_a parameter has been used as a predictor of the ability of titanium dental implants to induce interfacial shear strength. Systematic studies of blasted titanium implants with various surface roughness showed that a S_a value of 1.5 µm induces the highest RTQ values [26,51,72,73]. In Paper II, a comparison of published S_a and RTQ values for physically (blasted) and chemically (HF treated, anodized, incorporated ions) modified surfaces was performed. For blasted surfaces, the RTQ increased with increased S_a up to 1.5 µm. However, for non-blasted surfaces, this relationship was not proved, which suggests that other properties than the topography e.g. chemical composition and electronic

properties, influences the interfacial shear strength. This will be further discussed in Chapter 4 and 5.

In Paper III, the mechanical interaction between the bone and implant was investigated. This study resulted in the development of the *Local Biomechanical model*, which evaluates the ability of different surface topographies to induce retention strength with the bone during RTQ situations. This model was developed by the use of solid mechanics and considers only the biomechanical influence on interfacial shear strength. By making assumptions such as 100% bone-implant contact and that no adherence or friction exists between the bone and implant, the main contribution to the shear strength was found to be the slope of the area of the topography, which withstands the bone during the shear moment. This slope was named the *mean slope* and gives a measure of the retention strength induced by the implant topography. The interfacial shear strength was found to be proportional to the *mean slope*, Paper III. A schematic diagram of the RTQ shear situation as considered in the *Local Biomechanical model* is illustrated in Figure 3-3 with arrows indicating the areas which resists the bone. The calculated interfacial shear strength for blasted samples showed similar trends as obtained *in vivo* by measuring RTQ values, Papers III and V. The *mean slope* showed linear relationship with the 3D-surface roughness parameter S_{dq}, which suggests that the S_{dq} can be used to predict the ability of a surface to induce retention with the bone. The same correlation between *mean slope*, S_{dq} and *in vivo* RTQ could be established for other blasted and chemically treated surfaces in Paper V, showing the robustness and validity of the *Local Biomechanical model*.

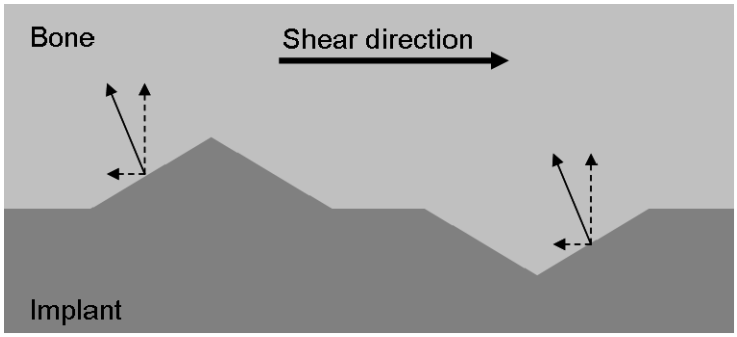

Figure 3-3. Illustration of the bone-implant interaction during the shear moment according to Local Biomechanical model. Arrows show the mean slope areas which influence the interfacial shear strength.

If the *mean slope* values obtained from the *Local Biomechanical model* are used to calculate the interfacial shear strength, unreasonably large values are obtained. This originates from the assumption of 100% bone-to-implant contact at fracture during the shear moment

and the fact that the elasticity properties of the implant and bone are neglected in the model. By introducing the elasticity of both bone and implant material and allowing for a gap to develop between the implant and bone during the RTQ situation, the *Local model* was further developed to the *Global Biomechanical model,* Paper IV. During the shear moment, compressive forces are induced which, due to the elasticity of both bone and implant material, pushes the materials away from each other leaving a gap between the implant surface and bone, Figure 3-4. This gap reduces the bone-implant contact ratio during the shear moment and lowers the calculated interfacial shear strength, which gives values more comparable to those obtained from RTQ studies than the *Local model*. The *Global Biomechanical model* showed that factors such as: *i)* implant surface roughness, *ii)* bone support and quality, *iii)* modulus of elasticity of the implant material, *vi)* implant diameter and *v)* wall thickness, all affect the gap size and therefore also the interfacial shear strength. The *Local* and *Global Biomechanical models* can be useful tools in the development of biomechanically optimized implant designs and surface topographies to specific bone anatomies and qualities, Papers III and IV. However, the contributions to interfacial shear strength from other surface modifications such as for example chemical composition and electronic properties of the surface oxide film are not considered in these models.

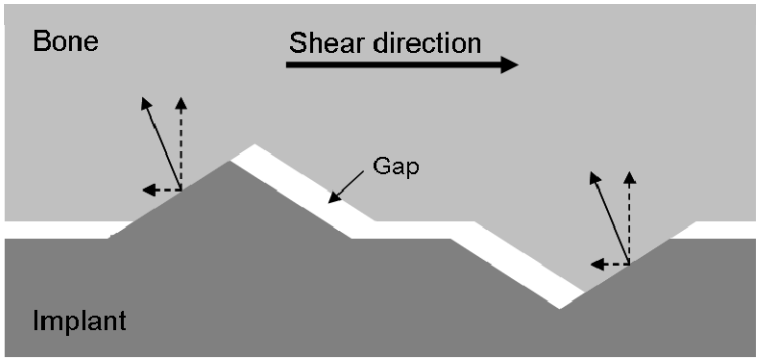

Figure 3-4. *Illustration of the bone-implant interaction considered in the Global Biomechanical model. Arrows indicate the areas giving the mechanical resistance immediately before fracture during the RTQ tests. The white areas show the gap induced by shear moment through compression of material and bone.*

3.2. Integrated Biomechanical and Topographical Surface Characterization (IBTSC)

In the previous sections, the value of using 3D-surface roughness parameters and the *Local* and *Global Biomechanical* models for describing the topographical and biomechanical effect on interfacial shear strength has been explained. Individually, these characterization

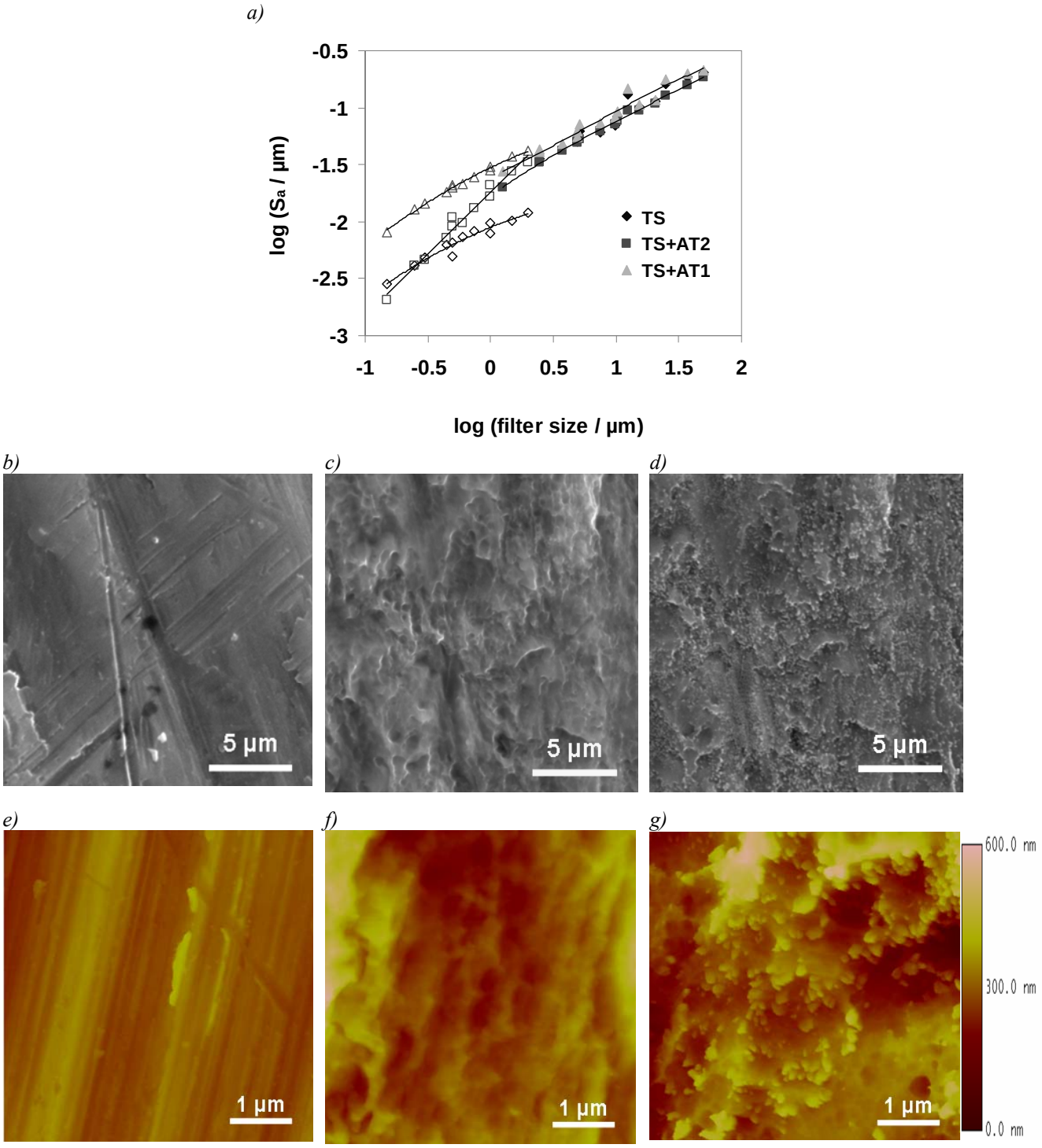

***Figure 3-5**. a) the S_a length-scale dependence for (b, e) turned surface, TS, treated with (c, f) oxalic acid, TS+AT2, and (d, g) a following treatment with diluted HF acid, TS+AT1. Filled symbols in the diagram represent values obtained in the 3D-SEM range while unfilled symbols show AFM results. SEM settings: ×5000 (103×78 µm), 30kV, WD = 10 mm (ESEM XL30). AFM settings: 5×5 µm, 0.8 Hz, 512 scan lines (Multimode SPM IIIa).*

techniques are good tools to evaluate the biomechanical properties of the surface topography on different levels. However, by combining them it is possible to identify topographies with specific positive effects on the interfacial shear strength, and the level at which these

topographies appear. This integrated way of analyzing the topography and its effects was called the *Integrated Biomechanical and Topographic Surface Characterization method* (IBTSC) and is discussed in detail in Paper V. The method can be used as a tool to create biomechanically optimized surfaces at all length scales. Further, with this method the topographical effects of a single preparation process can be evaluated. However, this is only possible if the same point of the surface is analyzed both before and after the actual treatment. If this is not ensured, natural variations instead of the influence of the surface treatments is likely to be measured.

In Papers II, III and V, the influence of chemical treatment and blasting on surface topography was evaluated. The chemical treatment using diluted HF acid induces nanoscaled surface features on both blasted and turned surfaces (Figure 3-2 and 5). This topographical change could not be observed within the 3D-SEM filter size range for the evaluated amplitude, spatial and volume parameters due to smoothening effects, Paper II. An example of this is given in Figure 3-5, where the S_a length-scale dependence for turned surface (b, e) treated with oxalic acid (c, f) and a following HF acid treatment (d, g) are shown. No differences could be observed in the range of the 3D-SEM filter sizes (filled symbols). However, by using AFM, the topographic differences of the surfaces are visualized and a separation in S_a values is obtained (unfilled symbols in Figure 3-5a). By AFM analysis, it is clearly shown that the oxalic acid and HF treatment induces sub-micro and nanosized surface features that influence the surface roughness, correctly analyzed in the AFM range.

As mentioned earlier, amplitude, spatial or volume parameters could not separate between turned and chemically treated surfaces in the 3D-SEM range. However, using the hybrid parameters (S_{dr} and S_{dq}) [31], separation between these two surfaces could be obtained as illustrated by the S_{dq} parameter in Figure 3-6. The relationship between S_{dq} and *mean slope* suggests that the turned surface treated with oxalic acid+HF (TS+AT1) would induce much larger retention strength than the oxalic acid treated (TS+AT2) and the untreated turned (TS) surface. In addition, when the same chemical treatments are performed on blasted surfaces, the *Local Biomechanical model* suggests that the largest retention strength would be obtained for the oxalic acid+HF treated surface (CB+AT1) followed by oxalic acid treated (CB+AT2) and untreated (CB) surface. This trend was also obtained *in vivo* [74]. The fact that S_{dq} and RTQ show the same trend could reduce the amount of animal studies needed to evaluate the performance of new implant topographies.

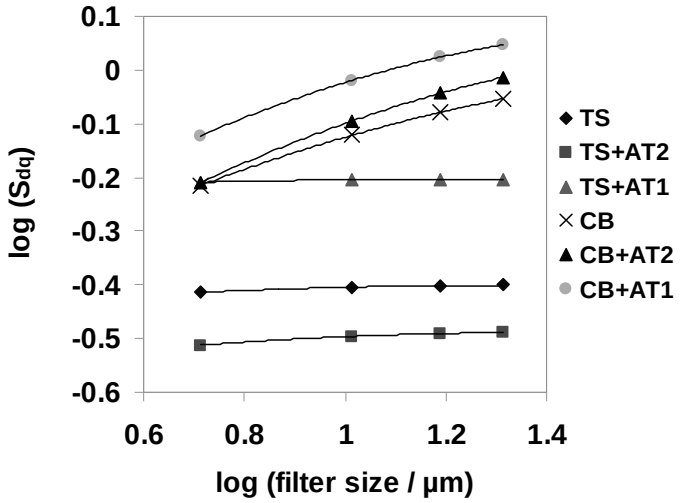

Figure 3-6. *S_{dq} parameter results for the surfaces shown in Figure 3-5 obtained at the 3D-SEM magnification of ×1200. TS show turned surface and CB coarse blasted surface. AT2 corresponds to chemical treatment with oxalic acid while AT1 is oxalic acid treatment with a follow up treatment in diluted HF acid.*

In this chapter a limited amount of surface roughness parameters have been discussed. The choice of parameters to be used when evaluating the topography of dental implants depends on the specific question at hand. For example, if the ability of topography to retain fluid is of interest, volume parameters should be used. However, if the total height of the topography is in question, amplitude parameters are most suitable. It is always recommended that complementary techniques and parameters are utilized since no single parameter nor technique can completely describe the complex topography of a dental implant surfaces alone [26,67,71]. From the findings of Papers II, III and V, it is recommended that an analysis of the length-scale dependence is performed to evaluate the full surface topography. By using the IBTSC method, the micro- to nanoscale topography is analyzed and a wide variety of 3D-SEM roughness parameters evaluated. This is necessary to give a detailed description of the complex topography of a dental implant and to be able to perform a correct interpretation of the topographical effect on the biological response.

4. MODIFICATION OF THE TITANIUM OXIDE FILM

In the previous chapter, the increased interfacial shear strength due to a roughened implant surface structure and the corresponding biomechanical stimulation was discussed. However, the biological responses to a titanium dental implant are also affected by material properties such as surface chemistry and composition [75]. Biocompatibility is a term used to describe the ability of a material to induce an appropriate host response [76]. For titanium, the biocompatibility has been attributed to the thin (2-5 nm) titanium oxide film naturally formed in air thus preventing the underlying metal against corrosion [10,11,77,78]. Although the naturally formed oxide film is proved to be well suited for the human body, numerous studies have been performed to modify the chemical composition and structure of this oxide in order to create a more bioactive material for dental implant applications. Improved bone response has for example been obtained by incorporation of biologically important ions such as Ca^{2+}, PO_4^{3-}, SO_4^{2-}, Mg^{2+}, F^- in the oxide or by covering the oxide with different kinds of coatings [13-15,78-82]. Using these surface modifications, substantial improvement in the biological performance has been reported and related to enhanced surface roughness and increased adsorption of specific blood serum proteins. However, only a limited number of studies consider the influence on the electronic properties of the oxide due to performed surface modification [19-21]. This chapter focuses on the electronic properties of the titanium oxide film and how these properties are affected when the surface is modified using various techniques. In addition, the effect of electronically altered surfaces on cellular response is also discussed.

4.1. Semiconducting properties of titanium dioxide

Titanium dioxide (TiO_2) is a semiconductor and has intermediate electric conductivity as compared to a metal and an insulator. The electric conductivity of a material depends on the valence- and conducting band and the gap between these in the energy band structure. TiO_2 is an ionic semiconductor where the valence band is mainly provided by the 2p orbitals of

oxygen and the conduction band from the 3d orbitals of titanium [83]. The semiconducting behaviour of TiO_2 is n-type, which means that it has an excess of negative charge carries i.e. an excess of electrons. This is due to the defect crystal structure, TiO_{2-x}, where the oxygen content decides the defect level and the electronic properties of the material. The levels of defects can be altered by changing the growth conditions for the oxide film [84-87]. Figure 4-1a shows a schematic picture of the band structure for a typical n-type semiconductor where the Fermi level (E_F) is situated closer to the conduction band (E_{CB}) than the valence band (E_{VB}).

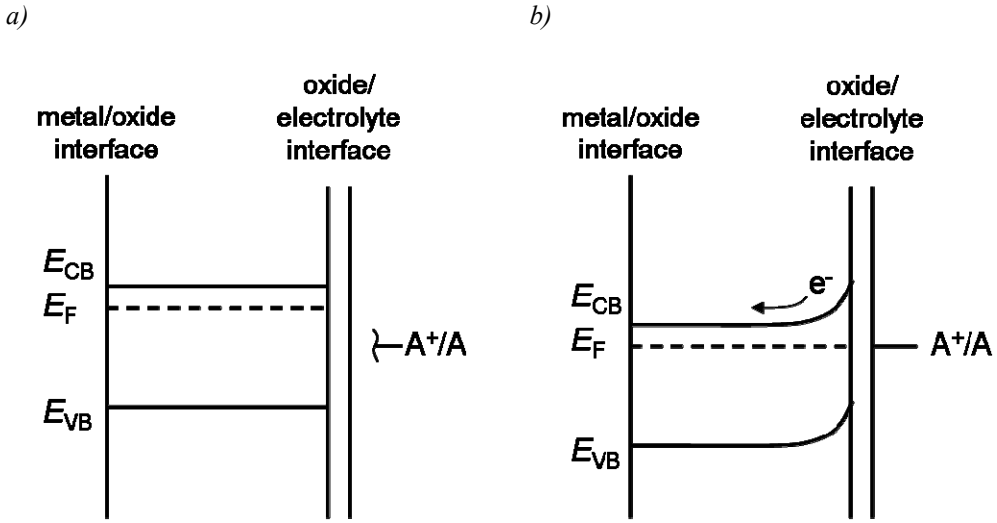

***Figure 4-1**. a) band structure of an n-type semiconductor before contact with electrolyte. A^+/A shows the potential for the redox couple in solution. b) band structure of the semiconductor after contact with electrolyte. E_{CB} and E_{VB} show the conduction and valence bands, respectively. E_F is the Fermi-level of the semiconductor.*

When a semiconductor is in contact with an electrolyte, the charge carriers are redistributed across the semiconductor/electrolyte interface until the Fermi-level is at the same potential as in the electrolyte. This is exemplified in Figure 4-1b where the potential at the solution side is given by the redox potential for A^+/A. The redistribution of the charge carriers creates a strong electric field and a depletion layer (space charge layer) is formed close to the oxide/solution interface. The size of the space charge layer and the strength of the electric field is dependent on the amount of defects in the semiconductor as well as on the dielectric constant and temperature [87]. The space charge capacitance (C_{sc}) contributes to the total capacitive behaviour of a semiconductor together with the capacitance of the double layer (C_{dl}) and of the oxide (C_{ox}), Equation 4-1.

$$\frac{1}{C_{tot}} = \frac{1}{C_{oxide}} + \frac{1}{C_{sc}} + \frac{1}{C_{dl}} \qquad \text{Equation 4-1}$$

The double layer is usually much larger than the space charge capacitance and can therefore be ignored. To measure the conductivity and defect level of a semiconductor, electrochemical impedance spectroscopy (EIS) can be used and this will be further described in Section 4.2.3.

4.2. Altering of the electronic properties of the titanium oxide film

As stated in the introduction to this chapter, the composition and chemistry of the material are factors, which influence the biological response. By using various surface modification techniques, the biological affinity of the TiO_2 film can be improved. Blasting and hydrofluoric acid (HF) treatment of titanium surfaces are two examples of successful modifications showing increased osseointegration and thrombogenicity compared to smooth or chemically untreated surfaces [14,56,81,88]. This has been explained by improved surface topography and surface chemistry. However, the results from Paper I show that both blasting and HF treatment generate changes in the electric properties of the titanium oxide and this could be a contributing factor to the increased biocompatibility observed for the actual surfaces [88,89]. Blasting induces distortions in the oxide structure and this results in increased numbers of charge carriers and a more conducting film, Paper I. The additional HF treatment increases the level of donor densities even further due to incorporation of fluoride ions (F^-) in the oxide structure through the exchange reaction shown in Equation 4-2, Paper I.

$$\equiv TiOH_2^+ + F^- \leftrightarrow \equiv TiF + H_2O \quad \text{where} \quad pH < pH_{pzc} \qquad \text{Equation 4-2}$$

pH_{pzc} is the point of zero charge and represents the pH where the net charge is zero. When an implant is surgically placed *in vivo*, a decrease in pH due to minor inflammation is induced. By introducing fluoride ions into the oxide structure, the pH_{pzc} of the titanium oxide film is decreased which means that the positive charge of the oxide film at acidic pH also decreases due to formation of TiF groups (Equation 4-2). This reduces the electrostatic repulsion between the titanium oxide and positively charged cations and plasmaproteins e.g. Ca^{2+} and fibrinogen, which are important for new bone formation [39,90]. An enhanced adsorption of both Ca^{2+} and fibrinogen are believed to be beneficial for triggering blood coagulation and the formation of new bone [39]. As the findings in Paper I show, the electronic properties of the outermost oxide film could enhance the osseointegration of a titanium dental implant. However, since the HF and blasting treatments both induces changes in electronic properties and topography it is impossible to establish the effect on biocompatibility from electronic properties solely. In Paper VI, an attempt to further investigate this relationship was

performed using titanium oxide films with different electronic properties but with the same topography. The following sections describe the preparation and topographic, chemical and electrical characteristics of the surfaces used in Paper VI.

4.2.1 Titanium oxide growth

In order to create samples with different electronic properties but with a minimal change in topography, galvanostatic anodization was used in Paper VI. Anodization is an electrochemical technique where a potential (potentiostatic anodization) or current (galvanostatic anodization) is applied over a metal forcing the oxide to grow. The oxide growth reaction for titanium dioxide (TiO_2) is shown in Equation 4-3 [85].

$$Ti + 2H_2O = TiO_2 + 4H^+ + 4e^- \qquad \text{Equation 4-3}$$

Titanium oxide growth takes place both at the metal/oxide and oxide/solution interfaces due to the applied field. The field strength decreases as the oxide film is growing and the oxide growth is stopped when the field strength is to low to promote ion migration through the film. Anodization has been used for many years in dental implant applications, preferably to create an altered surface topography. If high potentials or currents are used e.g. 100 V, 100 mA or higher, the change in topography is due to the vigorous oxygen evolution. The formed oxygen breaks through the oxide film and creates pores in the surface structure that has shown to iprove the osseointegration and cell response [91-93]. The pore size and the thickness of the oxide are affected by for example the concentration of the electrolyte and the magnitude of the applied field [94-98]. One example of an implant having a pore-structured surface induced by anodization is the commercially available TiUnite™ implant (Nobel Biocare) [86,93]. If the applied potential or current is low, the oxygen formation at the metal/oxide interface is moderate and the oxide grows according to Equation 4-3 without inducing pore structured surfaces. This method was used in Paper VI, and will be comprehensively described in the next section, 4.2.2

4.2.2 Galvanostatic anodization of titanium oxide

Galvanostatic anodization using low current densities was, in Paper VI, used for two different purposes *i)* preparation of titanium oxide films with different electronic properties but with minimal changes in topography and *ii)* to illustrate changes in the electronic properties of the titanium oxide, Paper VI. In the preparation part, three different current densities were used i.e. 2.4, 4.8 and 11.9 $mVcm^{-2}$ and the oxide film growth was continued until a potential of

20V was reached. By ending the anodization at the same potential, oxides with similar thicknesses were expected [85]. The anodization induced formation of a thicker oxide film, which can be observed by a colour shift from greyish to light (2.4 $mVcm^{-2}$) or dark (4.8 and 11.9 $mVcm^{-2}$) blue. Topographical analysis of the anodized samples using AFM and MeX® showed only small changes in surface morphology and roughness, Figure 4-2 and Table 4-1. Further, the anodization did not induce any changes in surface energy calculated from contact angle measurements.

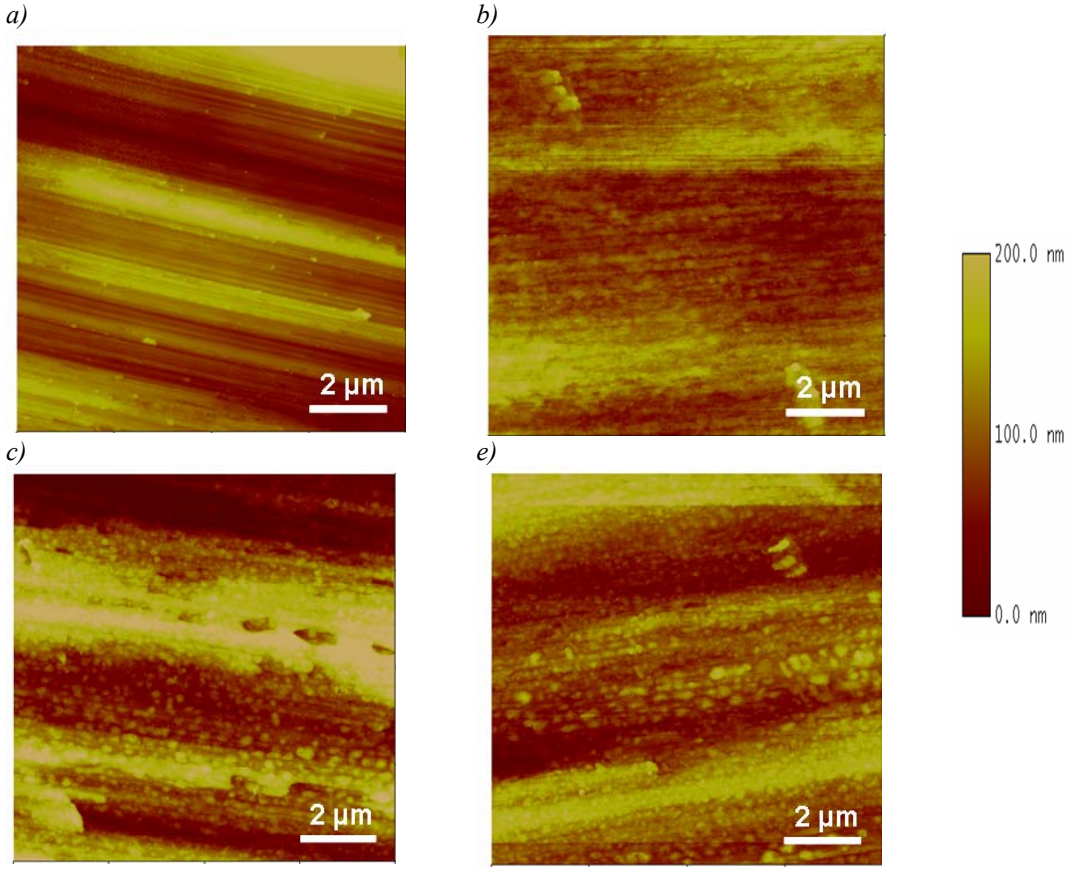

Figure 4-2. *AFM images of the turned surfaces before and after anodization to 20V of turned surfaces. a) reference (TS), anodization currents of b) 2.4, c) 4.8 and d) 11.9 $mAcm^{-2}$. AFM settings; 10×10 µm, 0.8 Hz, 512 scan lines (Multimode SPM IIIa),*

Table 4-1*. Surface roughness parameters for the reference (TS) and anodized surfaces analyzed in Paper VI. Surface roughness parameters are calculated from AFM measurements at 10x10 µm scan size and after applying a filter of 1.992 µm (corresponds to 20 % of the horizontal length of the scan size)*

	TS		**2.4 $mVcm^{-2}$**		**4.8 $mVcm^{-2}$**		**11.9 $mVcm^{-2}$**	
	average	*stdev*	*average*	*stdev*	*average*	*stdev*	*average*	*stdev*
S_a (nm)	11.36	1.19	11.94	0.01	15.74	0.60	16.01	1.57
S_{10z} (nm)	124.96	13.77	193.50	7.38	239.45	50.73	193.08	45.03
S_{dq}	0.25	0.07	0.37	0.05	0.38	0.02	0.39	0.02
S_{dr} (%)	3.52	1.49	7.11	2.07	7.08	0.92	7.41	0.64
V_{mc} (ml/cm^2)	123.67	11.15	132.50	0.71	171.00	6.93	172.25	15.61

For the other purpose, the galvanostatic anodization procedure was used to study how the electronic properties of the oxide changes as a function of current density. Time to reach the predetermined potential decreased with increasing current density, Figure 4-3. A continuous increase in potential with time was obtained for the two highest current densities, 4.8 and 11.9 $mVcm^{-2}$, while the anodization curve obtained with 2.4 $mVcm^{-2}$ had a different appearance. This curve indicates a local potential maximum between regions with different slopes, Figure 4-3. The local maximum has been described in the literature as representing a change either in growth efficiency or anodization ratio and the width of the local maximum indicate if the change is sudden (narrow maximum) or gradual (broad maximum) [99]. The total charge involved in the oxide growth up to 20 V was calculated to approximately 80 $mCcm^{-2}$ for the surfaces anodized with 4.8 and 11.9 $mVcm^{-2}$. For the surfaces anodized with 2.4 $mVcm^{-2}$, the amount of charge was significantly higher, approximately 1 Ccm^{-2}, and indicates that oxygen evolution occurs to a higher extent when oxides are growth by using 2.4 $mVcm^{-2}$ compared to 4.8 and 11.9 $mVcm^{-2}$. From the various slopes of the V/t curves for the anodized samples with different current densities, Figure 4-3, the growth efficiency (η, %) can be calculated through Equation 4-4 (assuming that the anodization ratio (*AR*) is constant) [99].

$$\left(\frac{\mathrm{d}V}{\mathrm{d}t}\right)_{\mathrm{j}} = \frac{M_{\mathrm{w}}}{zF \times \rho}\left(\frac{\eta}{AR}\right)_{\mathrm{j}} \times i_{\mathrm{tot}} \qquad \text{Equation 4-4}$$

where *AR* was assumed to be 2.0 nm/V, M_w and ρ the molar weight and density of TiO_2, i_{tot} the total current, *z* the metal valence and *F* is Faradays constant.

The anodization curves for the surfaces anodized with 2.4, 4.8 and 11.9 $mVcm^{-2}$ in Paper VI, show all an immediate increase in potential to approximately 1.6 V, Figure 4-3. This increase is attributed to the thin naturally formed oxide film of TiO_2. By plotting the following V/t slopes of the anodization curves, a growth efficiency of 79 % was calculated by using Equation 4-4, assuming that the *AR* is constant. This growth efficiency was increased to 100 % when the V/t slopes close to 20 V were used. This shows that the local maximum in the anodization curve for the 2.4 $mVcm^{-2}$ marks the transition between oxide growth with simultaneous oxygen evolution (before maximum) and mainly oxide growth (after maximum). Since oxygen evolution takes place within the film while growing with 2 $mVcm^{-2}$, internal stresses and changes in the oxide structure are induced [99,100], which may create oxides with different properties as compared to oxide films grown by 4.8 and 11.9 $mVcm^{-2}$. No local maximum in anodization curves for oxides grown by 4.8 and 11.9 $mVcm^{-2}$ were

observed, Figure 4-3. However, if the anodization had continued to higher voltages a local maximum would have been seen also for the higher current densities [97].

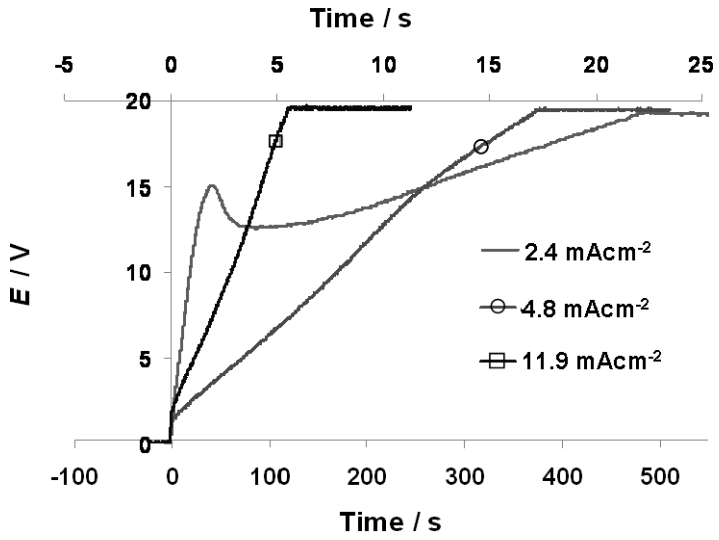

Figure 4-3. *Anodization curves for galvanostatic anodization of turned titanium discs using three different current densities. The time scale for 4.8 and 11.9 mVcm^{-2} is read on the top scale while the 2.4 mVcm^{-2} curve is read on the bottom scale.*

4.2.3 The effect on the oxide conductivity by anodization

Electrochemical Impedance Spectroscopy (EIS) was used to measure the conductivity and the amount of defects of the formed oxides in Paper VI, and the results are summaries in this section.

EIS measurements at open circuit potential (OCP) before and after anodization using different current densities are shown in Figure 4-4. At high frequencies, the obtained *log Z* values are related to the solution resistance, R_{sol}, of the cell and are independent of the analyzed sample i.e. same *log Z* values for all samples in Figure 4-4. With decreased frequency, the capacitive and resistive behaviour of the sample was measured and differences in both *log Z* and phase angles were measured for the anodized samples as compared to the untreated samples, Figure 4-4. An ideal capacitor would induce impedance data with a slope of -1 for the *log Z* vs *log f* curve and a phase angle of 90° for the same frequencies. However, real systems often show non-ideal capacitive behaviour comprising *log Z* slopes lower than -1 and phase angles lower than 90°, i.e. a frequency dependent capacitance. Reasons for such deviations are for example surface heterogeneities and inhomogeneous oxide properties,

which induce a distribution of time constants [101,102]. Non-ideal capacitive behaviour is observed for the natural TiO_2 oxide and as well as for the galvanostatically grown oxide films, Figure 4-4.

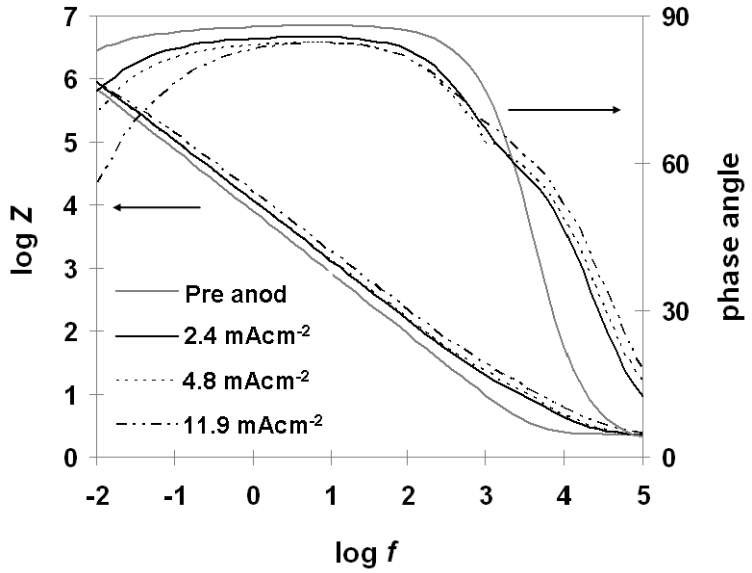

Figure 4-4. *Electrochemical impedance spectroscopy (EIS) data for the raw material (pre) and anodized surfaces measured at the open circuit potential.*

When modelling the EIS data to equivalent circuits, the non-ideal capacitive behaviour of the oxide films in Paper VI was simulated using Constant Phase Elements (CPE) which is placed in series with the solution resistance of the equivalent circuit, Figure 2-5. The fitting process gives values for the capacitance (Q) and frequency dispersion (α) for the CPE elements, which in turn can be used to calculate the effective (frequency independent) capacitance. Different models have been used to calculate the effective capacitance depending on the system studied [101,102]. It has been demonstrated that for lateral distribution of time constants the solution resistance is included in the calculations, while for a distribution of time constant perpendicular to the surface it can be omitted. For the system studied here, where an oxide is formed on the electrode surface, distribution of time constants occurs both laterally due to the roughness of the surface and perpendicularly due to inhomogeneous properties of the oxide. The effective capacitance was therefore calculated using Equation 4-5.

$$C_{\text{eff}} = Q^{1/\alpha}\left(\frac{1}{R_{\text{sol}}} + \frac{1}{R_{\text{oxide}}}\right)^{(1-\alpha)/\alpha} \qquad \text{Equation 4-5}$$

For the anodized samples in Paper VI, two time constants are observed (Figure 4-4), which is due to the formation of a layered oxide structure with an inner dense and an outer

more porous layer. Both the resistance and dielectric constant can vary within the layers and complicate the interpretation of the impedance data [101,103]. For example have dielectric constants between 20-170 been reported in literature [104,105].

To fit the EIS data for the anodized films presented in Figure 4-4, an equivalent circuit consisting of two CPE elements in series has to be used, Figure 2-1b. At OCP, the total capacitance of the oxide film is measured and is the sum of the inverse effective capacitances of the CPE elements in the equivalent circuit. Decreased capacitances were obtained for oxide films grown with increased current densities, shown in Figure 4-5. However, the anodization treatment significantly decreased the capacitance as compared to the naturally oxide film, shown as dotted line in Figure 4-5.

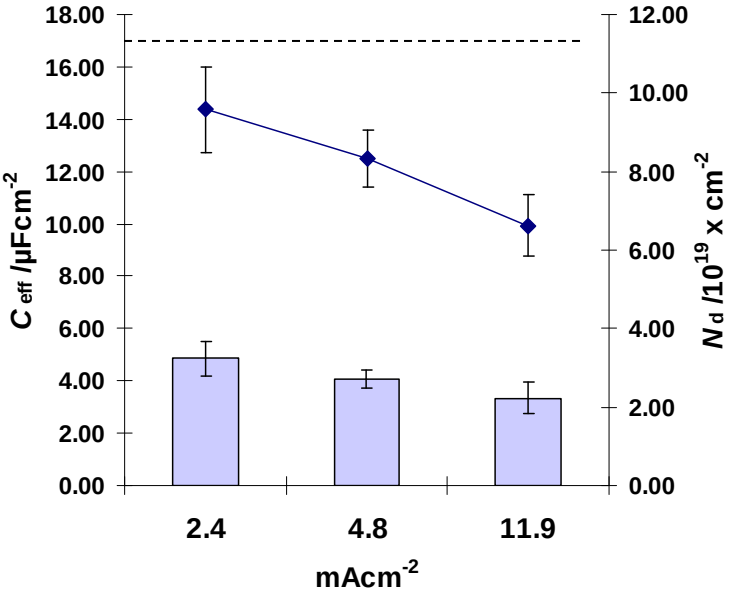

Figure 4-5. *Total capacitances and the standard devations for the surfaces anodized with 2.4, 4.8 and 11.9 mVcm^{-2} calculated from EIS data (Figure 4-4). The dotted line shows the capacitance for the natural oxide film. The points show the number of donor densities (N_d) calculated from Mott-Schottky (Figure 4-6).*

The amounts of charge carriers in the oxide were determined by impedance measurements utilizing Mott-Schottky analysis. In Paper VI the impedance response is measured at constant frequency during a linear potential sweep from +2 to 0 V. The capacitances are calculated using Equation 4-6 and C^{-2} is plotted as a function of applied potential, Figure 4-6.

$$C = \left(\frac{1}{\omega A Z''} \right) \qquad \text{Equation 4-6}$$

$\omega = 2\pi f$, where f is the frequency at which the analysis is performed. A is the geometric area and Z'' the imaginary part of the measured impedance.

a) *b)*

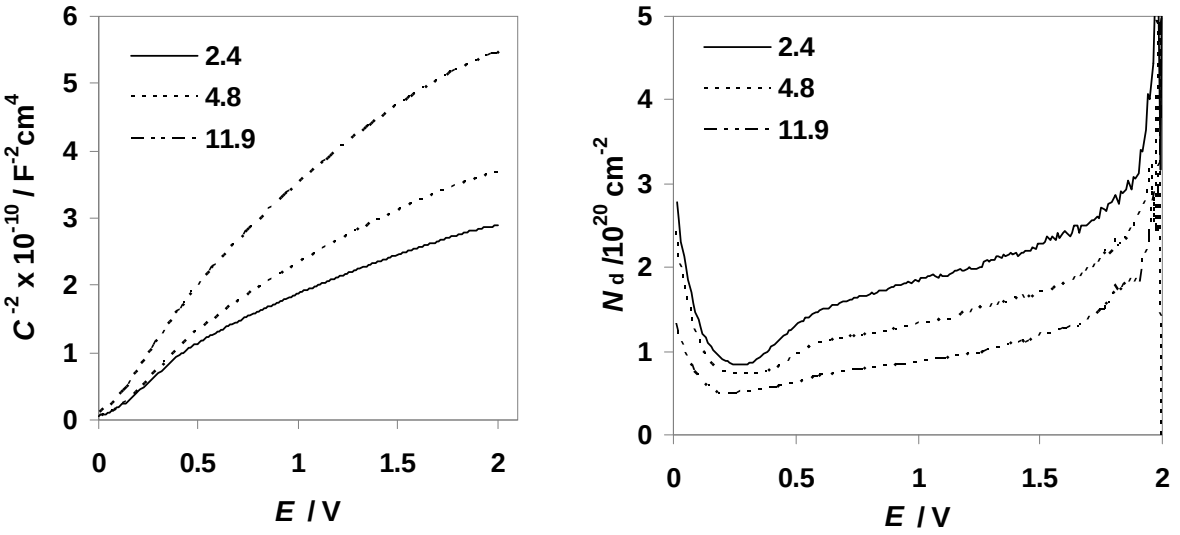

Figure 4-6. *a) Mott-Schottky curves for the anodized samples measured at 100Hz. b) Number of donor densities (N_d) calculated from the derivate of the Mott-Schottky curve.*

Linear C^{-2} vs E curves are expected for ideal semiconductors according to the Mott-Schottky relationship between the space charge capacitance and applied potential, Equation 2-1. The number of charge carriers (N_d) and the flatband potential (E_{fb}) can be determined from the slope and intercept of such plots (if C_{ox} and C_{dl} is assumed to be much larger than C_{sc}). The Mott-Schottky curves obtained were however non-linear, Figure 4-6, which indicates that the oxide film is layered with dissimilar capacitive behaviour [106]. The reasons for non-linearity of the Mott-Schottky curves have been related to inhomogeneous doping levels, irregularities of surface structure, changes in resistivity of the oxide film etc. [87,98,107,108], leading to a change in the number of charge carriers with potential. Non-linear Mott-Schottky curves are also typically observed for passive films where the semiconducting innermost layer is covered by a more resistive outer layer [87,106,107,109,110]. The capacitances measured for the anodized surfaces by Mott-Schottky at the higher potentials (Figure 4-6) are therefore the total capacitance obtained from both the space charge region and the insulating film. The number of donor densities (N_d) were calculated from the derivative of the non-linear Mott-Schottky curves in Paper VI and the results are shown in Figure 4-6b. For all anodized surfaces, the level of N_d decreases with decreased potential where highest donor densities were observed at the metal/oxide interface and lowest at the oxide/electrolyte. The donor density for the oxide can therefore be taken from the minimum in the N_d curve in Figure 4-6b where the capacitances in the Mott-Schottky curve is obtained from the oxide and double

layer. The number of charge carriers is decreasing with increasing anodization current density as shown in Figure 4-5 and shows that by growing oxides with 11.9 $mVcm^{-2}$, less conducting oxide films are formed. This is the same trend as observed in references [98] and [85]. From the region in the Mott-Schottky curve where constant N_d is shown, the flat band potential (E_{fb}) for the oxides were calculated and was found to be close to 0 V for the anodized surfaces**.**

4.3. Cellular response to oxide films with different electric properties

In order to investigate the influence of electronic properties on bone cell activity, osteoblastic cells (MG-63) were cultivated on the surfaces anodized with 2.4, 4.8 and 11.9 $mVcm^{-2}$, Paper VI. After 36 h cultivation, similar cell spreading and morphology were observed on the surfaces anodized with 2.4 and 4.8 $mVcm^{-2}$ as compared to the untreated surface, Figure 4-7a, b and c.

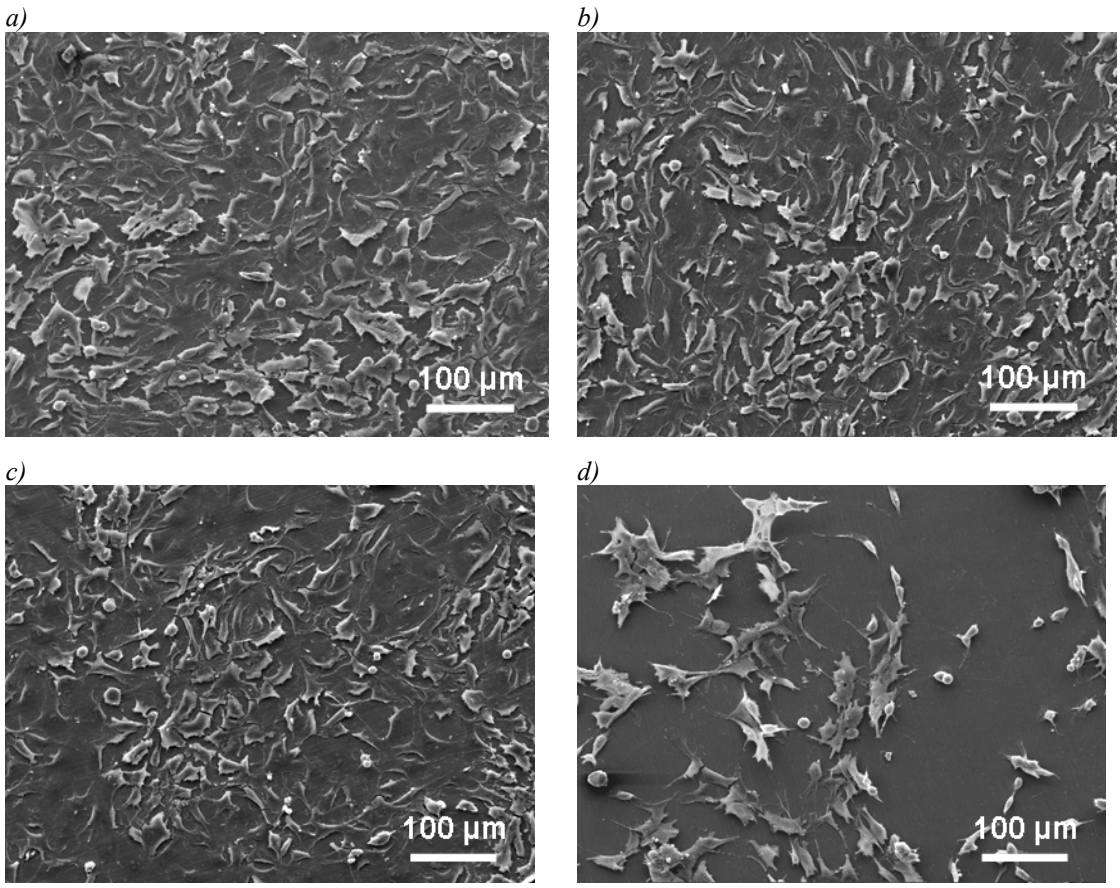

Figure 4-7. *SEM images showing the cell morphology and spreading on anodized samples after 36 h. a) Turned titanium disc reference (TS) anodized with b) 2.4, c) 4.8 and d) 11.9 $mVcm^{-2}$. SEM settings; SE detector, 30kV, WD = 10mm (XL30 ESEM).*

For the surface anodized with 11.9 $mVcm^{-2}$, decreased cell adhesion, decreased cell area and less cell extensions were observed. Through measurement of DNA content, the number of cells present on each sample were determined. After 7 days of cultivation, decreased cell numbers were found on the surface anodized with 11.9 $mVcm^{-2}$ as compared to the other surfaces and this trend was maintained after 14 days, Paper VI. However, the cells adherent to the surfaces anodized with 11.9 $mVcm^{-2}$ showed high mineralization activity but a somewhat delayed remodelling and decreased down regulation capacity of osteoclasts (ALP, PGE_2 and OPG), Paper VI.

Increased levels of adhered osteoblast and cellular response have been reported when surfaces exhibit a micro- and/or nanoroughened surface topography, high surface energy and wettability [94,95,111]. Explanations to this behaviour have been discussed in the terms of increased surface area, increased ability to adsorb important extracellular ions and proteins etc. Considering surface roughness and wettability, the highest number of adherent cells for the anodized surfaces in Paper VI would be expected for the surface with the largest roughness and with the highest surface energy. However, all anodized surfaces exhibited similar surface energies and the surface with the largest nanoroughness, measured for the surfaces anodized with 11.9 $mAcm^{-2}$, obtained the lowest cell numbers, Figure 4-7 and Paper VI. These results suggest that the electronic properties of the surfaces do have an effect on the cell response, and that this effect is superior to the contribution of small changes in the topography (Table 4-1). The surfaces were also immersed in simulated body fluid (SBF) mimicking the bioactivity of mineralization in bone, where anodization significantly increased the early formation of apatite. After longer times the effect of anodization was however diminished, Paper VI. Somewhat lower amounts of apatite were measured for the surface anodized with 11.9 $mVcm^{-2}$ after 1 week as compared to the reference and the other anodized surfaces, Paper VI. Based on the cell study and the SBF test, more conducting films seem to be preferable for dental implant applications. The effect on bioactivity by combining nanostructure and altered electronic properties will be discussed further in Chapter 5. This chapter will also include a more thorough description of the SBF method.

5. NANOSTRUCTURES

Nanotechnology has taken a prominent place in many research fields during the last 10 years due to the new physical and chemical material properties that this technique offers as compared to many conventional alternatives. Nanosized titanium dioxide (TiO_2) are used in a wide variety of applications from pharmaceuticals and paints to toothpaste and implants [112] where the concept of nano describes surface features of 100 nm or smaller. Nanostructures have been shown to induce increased cell adhesion and protein adsorption, which both are important for the osseointegration of dental implants [18,94,95]. The cell behaviour is also affected by the size, shape and distance between the nanostructures [113,114] giving an opportunity to design surfaces with optimized cell affinity. In previous chapters the effect of microtopography and electronic properties on the biocompatibility of titanium surfaces for dental implant applications have been discussed. The knowledge obtained from the biomechanical models in combination with the effects of electronic conductivity were, in Paper VII, used to design well characterized nanostructured surfaces with altered electronic properties. These surfaces were created by coating titanium discs with titanium dioxide nanoparticles of different sizes. In this chapter, the topographical and electronic properties of titanium dioxide (TiO_2) coated surfaces are evaluated.

5.1. TiO_2 nanoparticles

In Paper VII, spherical TiO_2 nanoparticles of three different sizes were spin-coated onto turned titanium discs in order to create nanostructured surfaces with altered electronic properties, Paper VII. The TiO_2 particles with the largest diameters were commercially available (Degussa P25) with an individual particle size in the range of 30-80 nm and 3:1 ratio of anatase and rutile, respectively [115]. The particle suspension of P25 particles used in Paper VII consisted of both individual particles and larger aggregates. In addition to the P25 particles, two smaller sizes of TiO_2 nanoparticles synthesized by controlled hydrolysis of $TiCl_4$ were used in Paper VII. By controlling reaction temperature, dialysis time/temperature

and storage time/temperature, TiO_2 nanoparticles of 22 and 8 nm in diameter were obtained [22]. The particles consisted predominately of anatase with only low traces of brookite. Detailed description regarding synthesis and characterization of the 8 and 22 nm particles can be found in [22]. Using spin coating, the particles were transferred from solution onto titanium discs with turned surfaces (TS surface used in Papers II, III and V).

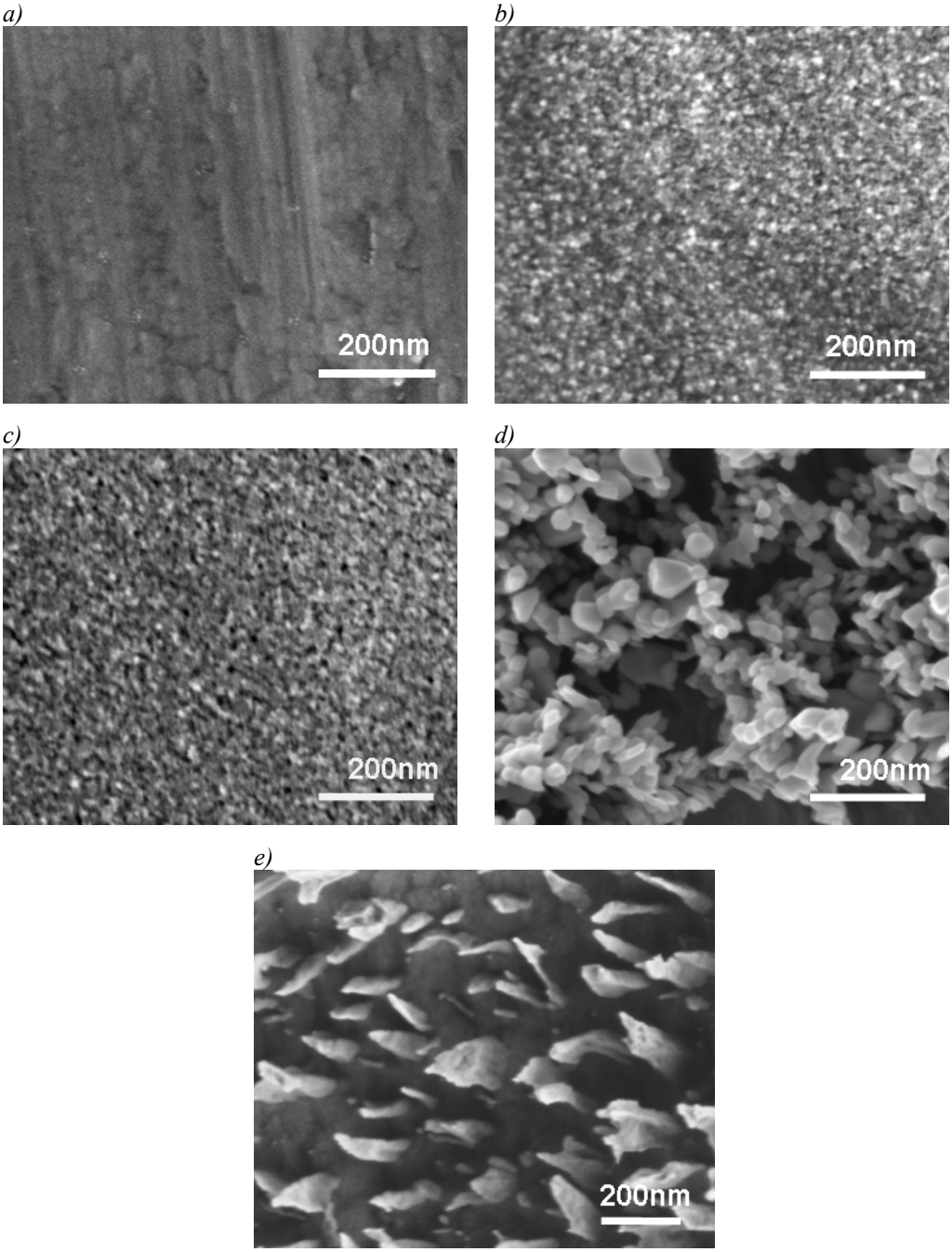

Figure 5-1. *SEM images on particle coated samples. a) Turned titanium surface (TS) coated with two layers of b) 8 nm particles, c) 22 nm particles, d) P25 (Degussa) and e) a turned titanium surface treated with oxalic acid and diluted HF acid sequentially (TS+AT1). SEM settings; In-Lense SE detector, 1 kV, WD 2.5 mm (Leo Ultra 55 FEG SEM)*

Figure 5-1 shows high-resolution SEM images of the reference (TS) surface coated with 8 nm (TS+8), 22 nm (TS+22) and commercial TiO_2 (TS+P25) particles. As a complement to the nanoparticle-coated surfaces, the nanostructured TS+AT1 (turned surface treated with oxalic acid and HF acid) surface were included in the study. The topography of this surface was evaluated in Paper V and the results showed that the treatments induce a hierarchically structured topography consisting of grooves and precipitated nanosized features, Paper V and [69], Figure 5-1e. The chemical composition and changes in electrochemical properties induced by the AT1 treatment have been discussed before [69]. In Paper VII, the coated and nanostructured surfaces were topographically, electrochemically and chemically evaluated and this as well as the effect on apatite formation in simulated body fluid (SBF) will be discussed in the following sections.

5.2. Topographical and chemical analysis

Topographical analysis of the coated and nanostructured surfaces was performed by AFM using overlapping scan sizes and a Gaussian filter of different sizes to obtain information of surface features in the range of 10 to 0.150 μm as described in Chapter 3. The coating with P25 particles (TS+P25) induced the largest changes in surface topography followed by the oxalic acid+HF treated surface (TS+AT1). This is illustrated in Figure 5-2 where the S_a (average height) and S_{dq} (root-mean-square of surface slope) parameters are plotted versus log filter size. Both coating with P25 particles and treatment according to AT1 (oxalic acid and HF) induced additional surface structures on top of the turned surface without fully covering it, Figure 5-1d and e, where the turned surface is shown as the darker areas. The coatings comprised of 8 and 22 nm particles (TS+8 and TS+22) completely covering the turned surface with particles, which in turn caused a decrease in surface roughness, Figure 5-2. Chemical analysis of the surfaces was performed by gracing-angle X-ray diffraction (GI-XRD). Besides titanium metal peaks, anatase and titanium-hydride peaks were identified for the TS+P25 and TS+AT1 surfaces, respectively. Only titanium metal peaks were obtained for the Ti+8 and Ti+22 samples, which show that the coatings are too thin to be measured by the GI-XRD. XRD patterns for the analyzed surfaces are shown in Figure 5-5 together with XRD patterns after SBF immersion.

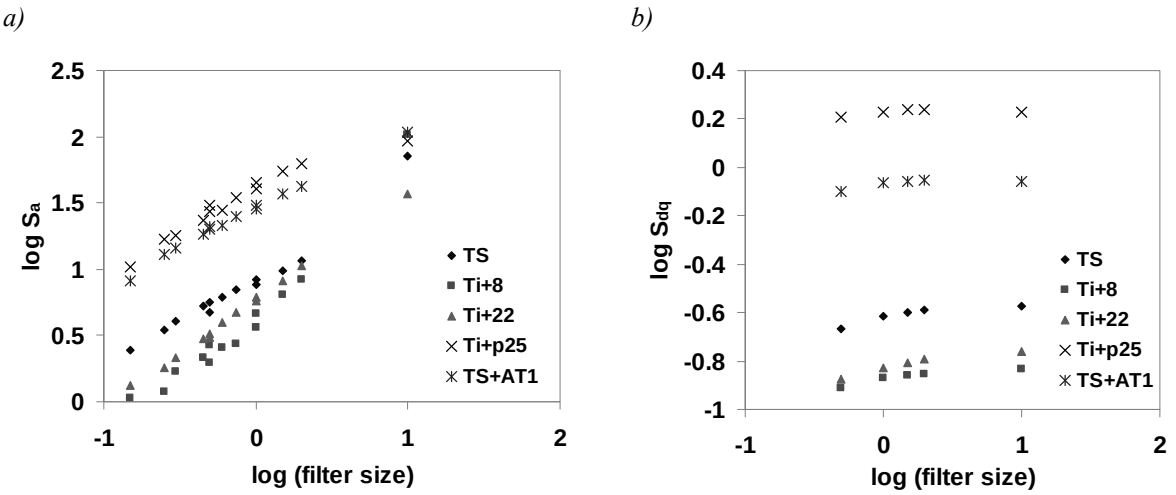

Figure 5-2. Length scale dependence for a) S_a (Average height) and b) S_{dq} (RMS-surface slope) surface roughness parameters measured on turned surfaces (TS) coated with 8 nm (TS+8), 22 nm (TS+22) and P25 (TS+P25) particles and treated with oxalic acid and diluted HF acid (TS+AT1). Analysis technique, AFM. Scan sizes a) 10×10, 5×5 and 3×3 µm and b) 10×10 µm. The points at the largest filter size corresponds to unfiltered values at 10×10 µm can size.

5.3. Electrochemical investigation of nanoparticles coated surfaces

In the present section, the electronic properties of the particle coated and nanostructured surfaces used in Paper VII are discussed. Spherical TiO_2 nanoparticles with a diameter less than 100 nm have increased reactivity as compared to titanium particles of larger sizes or to titanium materials with larger grain sizes. The higher reactivity is due to under-coordinated surface atoms induced by the curvature of the nanoparticles [116]. The electronic properties of the coated and nanostructured surfaces were studied by cyclic voltammetry (CV) Figure 5-3a. By scanning the potential in negative direction, the current injected into the oxide film is measured. When a more negative potential is applied, the Fermi level of the oxide film is shifted towards the conduction band and electrons can be injected into electronic traps situated just below the conduction band or defective surface sites within the TiO_2 band structure [117,118]. The reduction peak obtained at -0.89 V (Ag/AgCl, sat KCl) for the turned surface (TS) has been suggested to represent the filling of interstitial sites corresponding to the reduction of Ti(IV) to Ti(III) [119]. A corresponding but smaller oxidation peak is observed for the anodic sweep at somewhat higher potentials, inset in Figure 5-3a. This peak corresponds to partial emptying of the electronic trap. For the coated surfaces, the Ti(IV)/Ti(III) reduction peak is shifted towards more negative potential with decreased particle size. For the second scan the size of the reduction peak decreased for all samples but

most prominently for the 8 and 22 nm particle coated samples. This shows that most of the electrons are contained in the electronic traps and to fully empty these traps, more positive potentials would be necessary [118]. At more negative potentials, an exponential increase in current was observed for all surfaces, Figure 5-3a. This increase corresponds to the filling of energy levels close to the conducting band or to the filling of the conducting band [118,119], and not to hydrogen evolution since a symmetrical oxidation peak was observed, Figure 5-3a. The size of this peak is proportional to the active surface area of the electrodes [119] which increases with decreased particle size, Figure 5-3a. This trend is the opposite as obtained by AFM analysis where the TS+8 surface was identified as the surface with the lowest surface roughness followed by TS+22 and TS+P25 surfaces, Figure 5-2. The inconsistency between the CV and AFM trends show that the area measured by the AFM technique is the topographic area, which is not the same as the active area of the electrode as measured by CV.

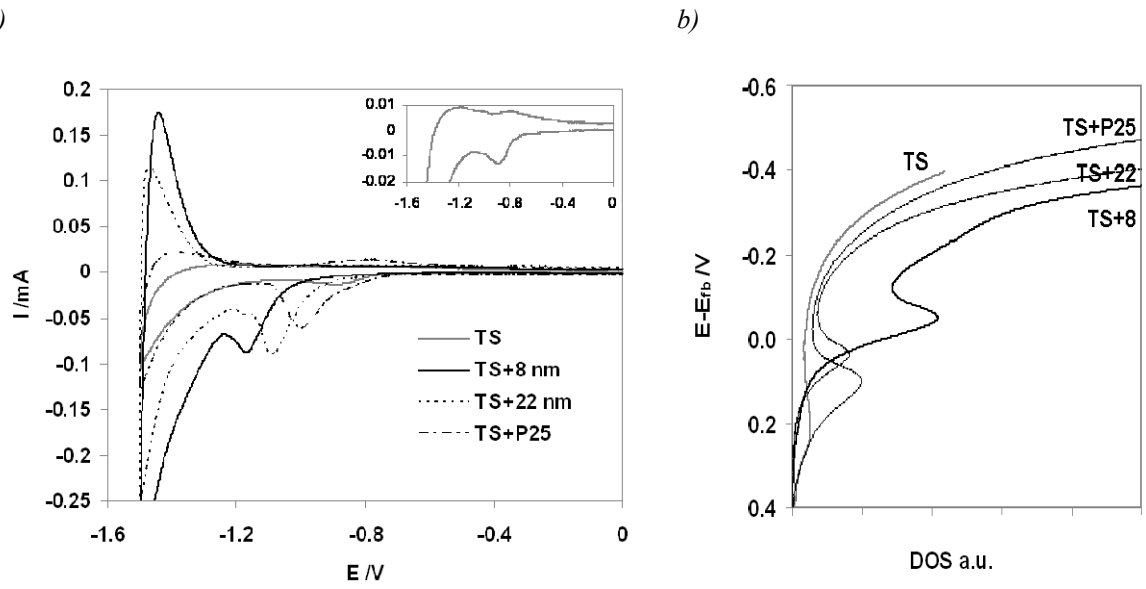

Figure 5-3. a) cyclic voltammogram for titanium discs with a turned surface (TS) coated with nanoparticles: 8 nm (TS+8), 22 nm (TS+22), P25 particles (TS+P25). TS+AT1 show CV for turned surface treated with oxalic acid and HF acid. In Figure b), the potential from the CV scan is plotted vs the calculated DOS for the reference and coated samples. CV's were performed in 0.1 M KOH with a sweep rate of 50 mVs^{-1}. The inset shows an enlargement of the CV for the TS surface.

5.3.1 Density of states (DOS)

The number of interstitial traps also called density of states (DOS) within the oxide film can be calculated from the reduction peaks in the CV scans by Equation 5-1.

$$g_0(-eE) = -\left[\frac{I}{eLAv}\right](\mathrm{eV}) \qquad \text{Equation 5-1}$$

where g_0 is the first estimate of the DOS in the band gap valid at zero Kelvin, L is the thickness of the film, I the current, A the electrode area, v the sweep rate, e the elementary charge, E the potential. Two peaks are observed in the cathodic scan for the coated samples *i)* an exponential tail of the conduction band, $g_{tail}(-eE)$, at the most negative potential and *ii)* a Gaussian-like distribution of the DOS, $g_{gauss}(-eE)$. The DOS in the exponential tail corresponds to the filling of states close to the conduction band while the Gaussian-like distribution corresponds to the filling of states within the band gap and the respectively DOS are calculated according to Equations 5-2 and 5-3 [118].

$$g_{tail}(-eE) = g_{tail,BE}\exp\left[\frac{-\alpha FE}{RT}\right] \qquad \text{Equation 5-2}$$

where $g_{tail,BE}$ is the DOS at the edge of the conduction band and α is related to the extension of the tail into the band gap.

$$g_{gauss}(-eE) = g_{gauss,sat} \times \frac{\exp\left[-(E-E_p)^2/2\sigma^2\right]}{\sigma\sqrt{2\pi}} \qquad \text{Equation 5-3}$$

where $g_{tail,BE}$ corresponds to the complete filling of interstitial states in the band gap, E_p is the peak potential and σ the standard deviation about the peak potential.

The calculated DOS are plotted vs the potential (E-E_{fb}) to visualize the position of DOS in relationship to the Fermi-level, here calculated to -1.1 V from the experiments in acid solution, Figure 5-3b. As seen in the Figure, the calculated interstitial DOS levels are positioned at different potentials for the samples where the TS surface has DOS levels at energies furthest below the Fermi-level followed by the TS+P25 and TS+22 surfaces, which maximum in interstitial DOS is close to the Fermi-level. The interstitial DOS for the surface coated with 8 nm particles are obtained at energies above the Fermi-level (at lower potentials) and also obtains the highest numbers of interstitial DOS. As also seen in Figure 5-3b, the filling of DOS within the exponential tail of the CV starts at different potentials for the surfaces in the order from lowest to highest potentials; TS+8<TS+22<TS+P25<TS. The amounts as well as at which potentials the DOS levels are obtained can alter the affinity of the surfaces for protein adsorption [19-21].

5.4. Simulated Body Fluid (SBF)

The biocompatibility of materials is closely related to the induced cellular response and protein adsorption. In addition, it has been suggested that the ability of a material to induce apatite nucleation is essential in order to form a strong bonding between a material and its surrounding [36]. To evaluate this ability, materials can be immersed in simulated body fluid (SBF). SBF is a synthetic solution with ion concentrations similar to that of human plasma and is supersaturated with respect to apatite. The hydroxylated form of apatite is called hydroxyapatite ($Ca_5(PO_4)_3OH$) and is an important mineral for the mechanical strength of bones [36,37]. Although the relationship between SBF test and *in vivo* has been questioned [120], the method is a useful tool for comparison the ability of different surfaces to induce apatite nucleation. The SBF method was used on the coated surfaces in Paper VII and the results are summarized here.

The coated and nanostructured surfaces in Paper VII were immersed in SBF solution for 12 h, 72 h, and 1 week at 37.0 °C and the amount of apatite formed was evaluated by EDX. Using the ratios of titanium signals measured for the samples after and before SBF immersion an indirect measure of the apatite coverage of the surfaces was obtained, Figure 5-4.

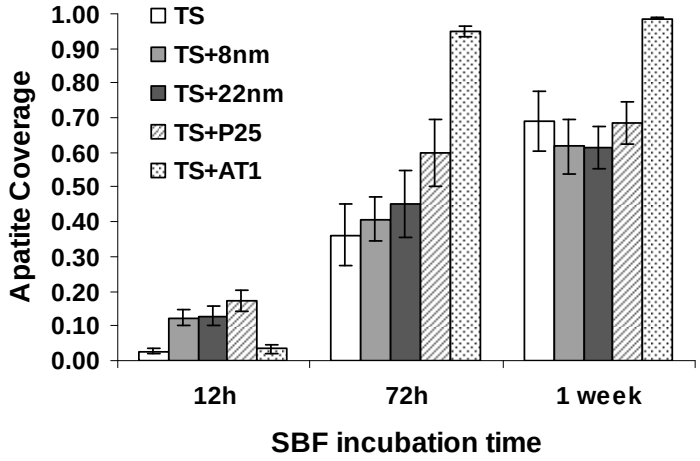

Figure 5-4. Calculated apatite coverage of the nanoparticles coated and nanostructured surfaces from EDX analysis after 12h, 72h and 1 week immersion in SBF, Paper VII. TS = turned surface, TS+8, 22 and P25 indicate surfaces coated with 8 nm, 22 nm and Degussa P25 particles. TS+AT1 show turned surface treated with oxalic acid and HF.

The particle-coated surfaces increased the early apatite formation as compared to the uncoated and nanostructured surfaces, Figure 5-4. However, after 72 h and 1 week, the uncoated reference surface obtained similar apatite coverage as the particle coated samples while the

TS+AT1 surface obtained the highest apatite coverage, Figure 5-4. The Ca/P ratios observed after 72 h were approximately 1.5 for all surfaces, indicating tricalciumphosphate ($Ca_3(PO_4)_2$), and was unchanged after 1 week immersion in SBF for all analysed surfaces. The crystallinity of the formed apatite layers was evaluated by GI-XRD. Traces of amorphous Ca-P compounds were detected after 1 week immersion in SBF on the TS, TS+8 on TS+22 surfaces, shown as a broad peak in the XRD pattern at 2Θ = 32 [121], in Figure 5-5a exemplified by the TS+22 surface. For the TS+AT1 surface where thick apatite layers were obtained already after 72 h immersion in SBF, peaks indicating crystalline Ca-P compounds were detected by XRD (2Θ = 26 - 32) [121,122], Figure 5-5b. The intensity of the peaks increased with time immersed in SBF solution.

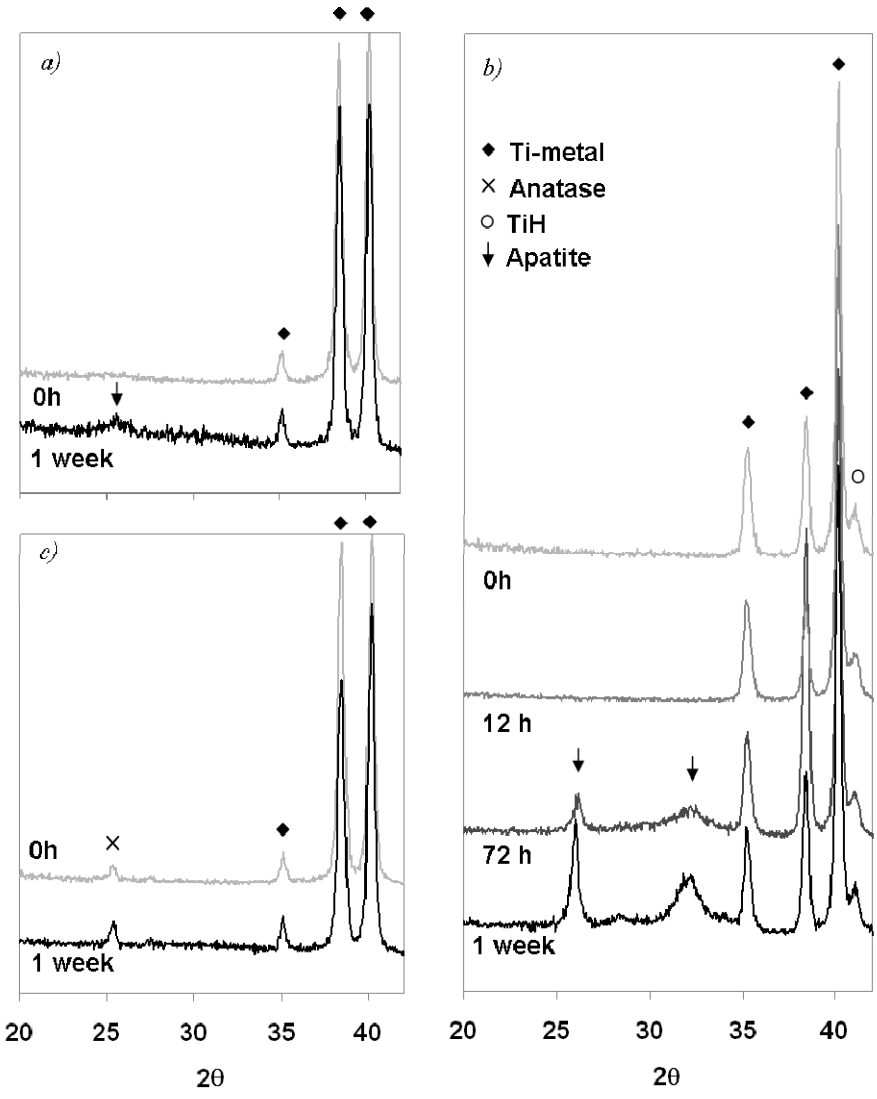

Figure 5-5. XRD patterns for the a) TS+22 and b) TS+P25 surfaces before (0 h) and after SBF immersion for 1 week. c) shows the XRD patterns for the TS+AT1 surface before (0 h) and after immersion in SBF for 12 h, 72 h and 1 week. Incident angle 5°. Peaks normalized to the largest Ti-metal peak.

In the XRD pattern of the TS+P25 surface, anatase peaks from the particles were obtained which is according to literature [115], Figure 5-5c. Despite that EDX analysis showed similar apatite coverage for the TS+P25 surface as for the TS+8 and TS+22 surfaces (Figure 5-4), no peaks corresponding to Ca-P compounds were detected by XRD, Figure 5-5c.

The morphology of the apatite layers was evaluated by SEM. Figure 5-6 illustrates SEM images of the coated and nanostructured surfaces after 1 week of immersion in SBF and shows that the morphology of the formed apatite layer is very different depending on the underlying surface.

The apatite layer obtained for the TS+AT1 surface (Figure 5-6e) is of similar morphology as can be seen in the literature on surfaces covered with a thick layer of apatite [36,123]. Cracks were observed within the apatite layer of the TS+AT1 surface and have been explained to be due to drying effects [16,124]. The morphology and thickness of the apatite layer on the TS, TS+8 and TS+22 samples are much thinner than observed on the TS+AT1 surface and show distinct cracks with small apatite crystals situated at certain places within the cracks, Figure 5-5a-c. The crystals were formed before the cracks as determined by SEM imaging after 12 and 72 h in SBF. The Ca/P ratio for the crystallites was 1.7 and indicates the formation of hydroxyapatite ($Ca_5(PO_4)_3OH$). Partially detachment of the apatite layers on the TS+8 and TS+22 surfaces are observed, Figure 5-6b and c, and could be due to the absence of surface roughness which is necessary to create a strong anchorage of the formed apatite layer [125,126]. Early nucleation of apatite crystals has been reported to increase on titanium surfaces comprised of anatase as compared to amorphous titanium [16,127]. This could explain the earlier apatite nucleation observed for the surfaces coated with 8 and 22 nm particles, predominantly of anatase phase [22], compared to the TS and TS+AT1 surfaces. The combination of anatase phase and higher surface roughness can explain the higher apatite coverage obtained for the TS+P25 surface at all SBF immersion times compared to the TS+8 and TS+22 surfaces, Figure 5-4.

5.5. Prospects of TiO_2 nanoparticles for dental implant applications

As stated in the introduction to this chapter, TiO_2 nanoparticles are used in a large variety of applications. Although the nanoparticles are non-toxic by themselves, the possible harmful effects on environment and health are now discussed. For orthopaedic implants micro- and nanosized particles can be induced by wear. Nanoparticles of these sizes have been shown to be taken up by cells and induce alteration of the cell function and the formation of giant cells

that in turn can give rise to osseointegration failure [128,129]. However, TiO_2 nanoparticles solely have been shown to decrease bacterial adhesion, which causes problems with adhesives and dental implants [130,131]. The results obtained in Paper VII, where coatings of TiO_2 nanoparticles clearly enhanced the early apatite formation, indicate that TiO_2 nanoparticles could be useful in dental implant applications although further investigations are necessary.

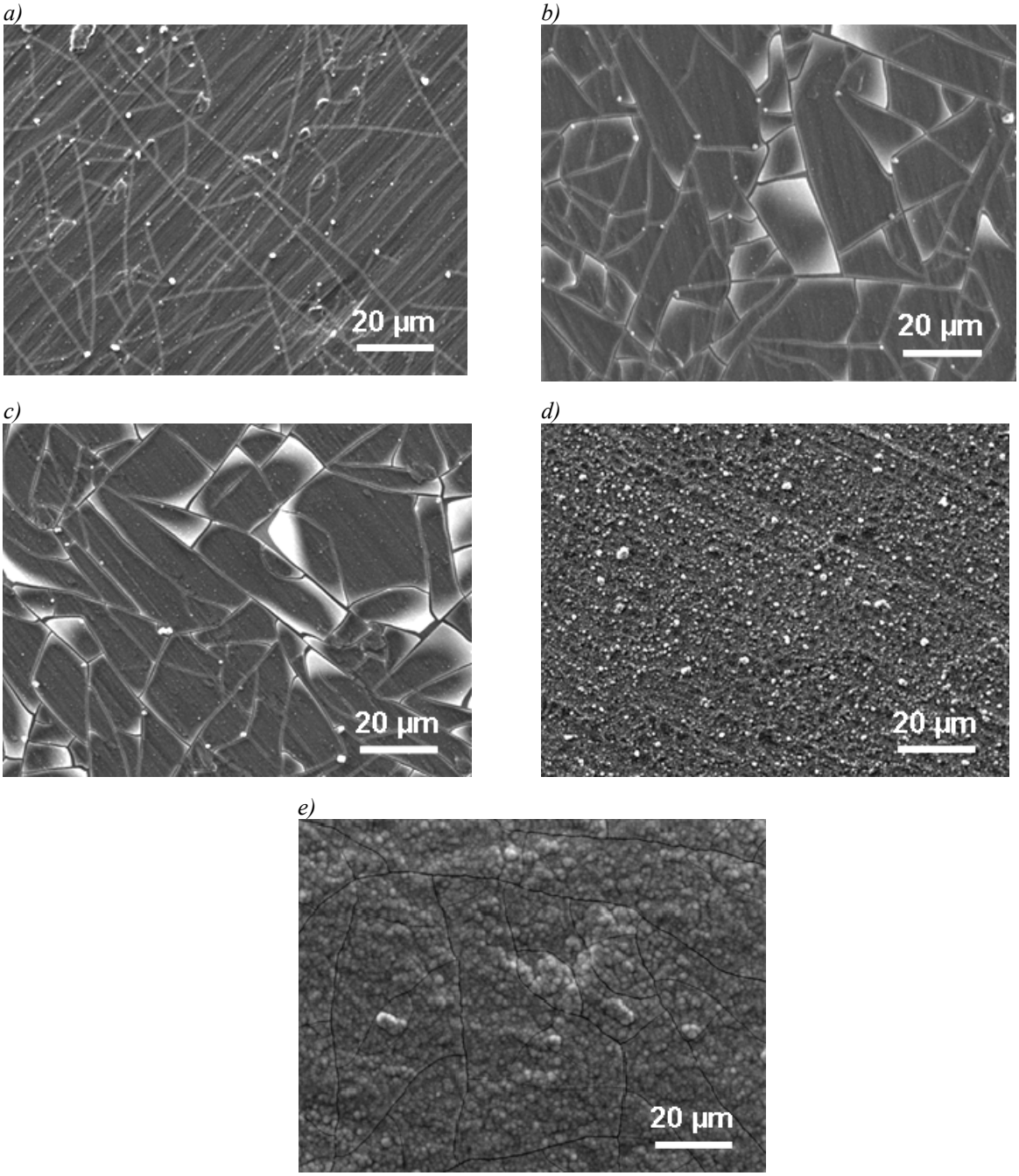

Figure 5-6. SEM images after immersion in SBF solution for 1 week. Titanium discs with a) turned surface (TS), b-d) coated surfaces with 8 nm (TS+8), 22 nm (TS+22) and P25 (TS+P25) particles. e) show turned surface treated with oxalic acid and diluted HF acid (TS+AT1). SEM settings; ×1000, 10 kV, WD 10 mm (ESEM XL30).

6. CONCLUSIONS AND FUTURE ASPECTS

- An integrated concept for surface characterization was developed – IBTSC (Integrated Biomechanical and Topographic Surface Characterization) and can be used to evaluate the topographical changes induced by sequential process steps. This concept is an excellent tool when developing new surfaces with biomechanically optimized surface topography.

  To further investigate the applicability of the IBTSC concept, the model will be applied on additional surface structures.

- An improved understanding of the biomechanical properties was gained by simulating the interfacial shear strength of model and real implant surfaces. A simple relationship between surface roughness and interfacial shear strength was established and is integrated in the IBTSC approach. Besides the surface roughness, bone quality and implant design were shown to be important.

- Alteration of the electronic properties of TiO_2 film had a larger influence on cellular attachment and early apatite nucleation than a small change in surface topography. Based on these results, thin and more conducting oxide films with a high level of defects seem to be preferable for dental implant applications.

  To establish the relationship between altered electronic properties and biological response further investigations of anodized samples by for example cell studies and protein experiments are necessary.

- TiO_2 nanoparticle coated samples induce an altered surface reactivity as compared to the uncoated reference. The coatings significantly increased the early nucleation of apatite, which indicates a more bioactive surface.

  Studies of protein adsorption on the coated samples would give further information regarding the effect of TiO_2 nanoparticles on the early biological response.

  By altering the coating thickness and preparation conditions, such as temperature, the interaction strength between the underlying substrate and the nanoparticles as well as particle-particle interaction can be improved.

7. ACKNOWLEDGEMENT

This work was performed in collaboration between Gothenburg University and Astra Tech AB. Financial support from Swedish Research Council is gratefully acknowledged.

I want to express my appreciation and gratitude to my supervisor Prof. Elisabet Ahlberg for all support and encouragement and for sharing her knowledge and enthusiasm. These years have been hard work but a lot of fun.

I also would like to show my sincere appreciation to my co-supervisor Dr. Ingela Mattisson for all her encouragement and support and for holding on to the red thread when I occasionally misplaced it. Thank you!

I also want to acknowledge my co-supervisor Dr. Stig Hansson for his enthusiasm and the fruitful discussions we had during the years and will hopefully continue to have.

Many thanks to all my colleagues at the RI department at Astra Tech and especially the members of the RTD group for all their support: Kristina JB, Anna, Christina, Kristina B, Monja, Stefan, Frida, Anders, Jeanette and Anette.

A big thank you to all present and former colleagues of the Electrochemistry group at the Gothenburg University; Angelica, Anders, Annika, Alexander, Gert, Jakub, Kristoffer, Michael, Patrick, Zareen, and of course my close companion and room-mate from the start – Jenny.

Special thanks to: Stefan Johnsson for helping me with sample material at stressful and critical moments, Christina Gretzer and Anna Arvidsson for helping we with cell and SBF studies and for the fruitful discussions, Jenny Perez-Holmberg for supplying me with the TiO_2 nanoparticles, Patrick Steegstra for help with acquiring SEM images, Roger Saghdal and Esa Vähänen for support from the workshop concerning electrical and mechanical issues.

All my love and thanks to my friends and special thanks to Roger, Anna-Karin and Jonas for being there and reminding me that there is a world outside the lab and thank you Zoey for letting me “use” you ☺

Till familjen: Tack mamma och pappa för att ni alltid har trott på mig och stöttat mina idéer och planer. Och tack pappa för alla körda flyttlass genom åren. Tack Elias för att jag får

vara med och spela innebandy och för att jag får bygga snögrottor när jag behöver en rast från datorn. Massor med kramar och tack till min syster Pamilla för att du hejar på mig och kommer med kloka råd. Tillsist vill jag tacka Uffe för ditt lugn och tålamod, din humor och din kärlek. Jag älskar dig.

Future – here I come!

8. REFERENCES

1. Shalabi MM, Gortemaker A, Van't Hof MA, Jansen JA, Creugers NHJ. *Implant surface roughness and bone healing: a systematic review*. J. Dent. Res. 2006;85:496-500.
2. Albrektsson T, Albrektsson B. *Osseointegration of bone implants. A review of an alternative mode of fixation*. Acta. Orthop. Scand. 1987;58:567-577.
3. Gotfredsen K, Nimb L, Hjorting-Hansen E, Jensen JS, Holmen A. *Histomorphometric and removal torque analysis for TiO_2-blasted titanium implants. An experimental study on dogs*. Clin. Oral. Impl. Res. 1992;3:77-84.
4. Vogel V, Sheetz M. *Local force and geometry sensing regulate cell function*. Nat Rev Mol Cell. Biol. 2006;7:265-275.
5. Adachi T, Sato K, Higashi N, Tomita Y, Hojo M. *Simultaneous observation of calcium signalling response and membrane deformation due to localized mechanical stimulus in single osteoblast-like cells*. J Mech. Behav. Biomed. Mater. 2008;1:43-50.
6. Iqbal J, Zaidi M. *Molecular regulation of mechanotransduction*. Biochem. Biophys. Res. Co. 2005;328:751-755.
7. Hansson S. *Toward an optimized dental implant design*. In: Ellingsen JE, Lyngstadaas SP, editors. Bio-implant interface. Boca Raton: CRC Press, 2003. p. 29-42.
8. Brunski JB. *In vivo bone response to biomechanical loading at the bone/dental-implant interface*. Adv. Dent. Res. 1999;13:99-119.
9. Frost HM. *A 2003 update of bone physiology and Wolff´s law for clinicians*. Angle. Orthod. 2004;74:3-15.
10. Kasemo B, Lausmaa J. *Surface science aspects on inorganic biomaterials*. CRC. Crit. Rev. Biocompat. 1986;2:335-380.
11. de Jonge LT, Leeuwenburgh CG, Wolke JGC, Jansen JA. *Organic-inorganic surface modifications for titanium implant surfaces*. Pharmac. Res. 2008;25:2357-2369.
12. Sul YT, Johansson CB, Jeong Y, Roser K, Wennerberg A, Albrektsson T. *Oxidized implants and their influence on the bone response*. J. Mater. Sci.- Mater. Med. 2001;12:1025-1031.
13. Sul Y, Johansson Carina B, Kang Y, Jeon D, Albrektsson T. *Bone reactions to oxidized titanium implants with electrochemical anion sulphuric acid and phosphoric acid incorporation*. Clin. Implant. Dent. Relat. Res. 2002;4:78-87.
14. Cooper LF, Zhou Y, Takebe J, Guo J, Abron A, Holmen A, Ellingsen JE. *Fluoride modification effects on osteoblast behavior and bone formation at TiO_2 grit-blasted c.p. titanium endosseous implants*. Biomaterials 2006;27:926-936.
15. Nayab SN, Jones FH, Olsen I. *Effects of calcium ion implantation on human bone cell interaction with titanium*. Biomaterials 2005;26:4717-4727.
16. Chen X, Nouri A, Li Y, Lin J, Hodgson PD, Wen C. *Effect of surface roughness of Ti, Zr, and TiZr on apatite precipitation from simulated body fluid*. Biotechnol. Bioeng. 2008;101:378-387.
17. Webster TJ, Ejiofor JU. *Increased osteoblast adhesion on nanophase metals: Ti, Ti6Al4V, and CoCrMo*. Biomaterials 2004;25:4731-4739.

18. Divya R, Manzoor K, Menon D, Selvamurugan N. *The design of novel nanostructures on titanium by solution chemistry for an improved osteoblast response*. Nanotechnology 2009;20:195191-195202.
19. Huang N, Yang P, Cheng X, Leng Y, Zheng X, Cai G, Zhen Z, Zhang F, Chen Y, Liu X, Xi T. *Blood compatibility of amorphous titanium oxide films synthesized by ion beam enhanced deposition*. Biomaterials 1998;19:771-776.
20. Chen JY, Leng YX, Tian XB, Wang LP, Huang N, Chu PK, Yang P. *Antithrombogenic investigation of surface energy and optical bandgap and hemocompatibility mechanism of* $Ti(Ta^{+5})O_2$ *thin films*. Biomaterials 2002;23:2545-2552.
21. Huang N, Yang P, Leng YX, Chen JY, Sun H, Wang J, Wang GJ, Ding PD, Xi TF, Leng Y. *Hemocompatibility of titanium oxide films*. Biomaterials 2003;24:2177-2187.
22. Abbas Z, Holmberg JP, Hellström AK, Hagström M, Bergenholtz J, Hassellöv M, Ahlberg E. *Synthesis, characterization and particle size distribution of* TiO_2 *colloidal nanoparticles*. Colloids Surf A 2011;doi:10.1016/j.colsurfa.2011.03.064.
23. Orazem ME, Tribollet B. *Electrochemical impedance spectroscopy*. New Jersey: Wiley, 2008.
24. Binnig G, Quate CF, Gerberg C. *Atomic force microscopy*. Physical Review Letters 1986;56:930-934.
25. Thomas TR. *Rough surfaces*. 2nd Edition. London: Imperial College Press, 1999.
26. Wennerberg A, Albrektsson T. *Suggested guidelines for the topographic evaluation of implant surfaces*. Int J Oral Max Impl 2000;15:331-344.
27. Goldstein J, Newbury DE, Lyman C, Echlin P, Lifshin E, Sawyer L, Michael JR. *Scanning electron microscopy and X-ray microanalysis*. 3rd Edition. , 2003.
28. Ponz E, Ladaga JL, Bonetto RD. *Measuring surface topography with scanning electron microscopy. Part 1. EZEImage. A program to obtain 3D surface data*. Microsc. Microanal. 2006;12:170-177.
29. Alicona Imaging GmbH. MeX 5.0. 2007;5.0.
30. Löberg J. *Characterising dental implant surfaces by topographical, electrochemical and biomechanical Methods*. Licentiate thesis, University of Gothenburg, Sweden 2009:1-54.
31. Dong WP, Sullivan PJ, Stout KJ. *Comprehensive study of parameters for characterizing three-dimensional surface topography IV: Parameters for characterizing spatial and hybrid properties*. Wear 1994;178:45-60.
32. Dong WP, Sullivan PJ, Stout KJ. *Comprehensive study of parameters for characterizing three-dimensional surface topography III: Parameters for characterizing amplitude and some functional properties*. Wear 1994;178:29-43.
33. Stout KJ, editor. *Development of methods for the characterisation of roughness in three dimensions*. London: Penton Press, 2000.
34. Young VY, Hoflund GB. *Photoelectron spectroscopy (XPS and UPS), auger electronspectroscopy (AES), and ion scattering spectroscopy (ISS)*. In: Riviére JC, Myhra S, editors. Handbook of surface and interface analysis. Methods for problem-solving. 2nd Edition: CRC Press, 2010. p. 19-64.
35. Oyane A, Kim HM, Furuya T, Kokubo T, Miyazaki T, Nakamura T. *Preparation and assessment of revised simulated body fluids*. J. Biomed. Mater. Res. A 2003;65A:188-195.
36. Kokubo T, Takadama H. *How useful is SBF in predicting in vivo bone bioactivity?* Biomaterials 2006;27:2907-2915.
37. Fratzl P, Himadri SG. *Nanoscale mechanisms of bone deformation and fracture*. In: Bäuerlein E, editor. *Handbook of biomineralization. Biological aspects and structure* formation. Weinheim: Wiley-VCH, 2007. p. 397-414.
38. Rho J, Kuhn-Spearing L, Zioupos P. *Mechanical properties and the hierarchical structure of bone*. Med. Eng. Phys. 1998;20:92-102.

39. Davies JE. *Understanding Peri-Implant Endosseous Healing*. J. Dent. Education. 2003;67:932-949.
40. Hansson S, Werke M. *The implant thread as a retention element in cortical bone: the effect of thread size and thread profile: a finite element study*. J. Biomech. 2003;36:1247-1258.
41. Hansson S. *The implant neck: smooth or provided with retention elements. A biomechanical approach*. Clin. Oral. Impl. Res. 1999;10:394-405.
42. Steflik DE, Hanes PJ, Sisk AL, Parr GR, Song MJ, Lake FT, McKinney RV. *Transmission electron microscopic and high voltage electron microscopic observations of the bone and osteocyte activity adjacent to unloaded dental implants placed in dogs*. J. Periodontol. 1992;63:443-452.
43. Sennerby L, Thomsen P, Ericson LE. *Early tissue response to titanium implants inserted in rabbit cortical bone. Part II. Ultrastructural observations*. J. Mater. Sci.-Mater. M. 1993;4:494-502.
44. Puleo DA, Nanci A. *Understanding and controlling the bone-implant interface*. Biomaterials 1999;20:2311-2321.
45. Brunski JB, Puleo DA, Nanci A. *Biomaterials and Biomechanics of Oral and Maxillofacial Implants: Current Status and Future Developments*. Int. J. Oral. Max. Impl. 2000;15:15-46.
46. Stanford CM, Brand RA. *Toward an understanding of implant occlusion and strain adaptive bone modelling and remodelling*. J Prosthet Dent. 1999;1999:443-452.
47. Rubin C, Lanyon LE. *Regulation of bone formation by applied dynamic loads*. J. Bone. Joint. Surg. 1984;66:397-402.
48. Rubin CT, Sommerfeldt DW, Judex S, Qin YX. *Inhibition of osteopenia by low magnitude, high-frequency mechanical stimuli*. Drug. Discovery. Today. 2001;6:848-858.
49. Mosley JR, Lanyon LE. *Strain rate as a controlling influence on adaptive modeling in response to dynamic loading of the ulna in growing male rats*. Bone 1998;23:313-8.
50. Albrektsson T, Hansson HA, Ivarsson B. *Interface analysis of titanium and zirconium bone implants*. Biomaterials 1985;6:97-101.
51. Wennerberg A, Albrektsson T, Johansson C, Andersson B. *Experimental study of turned and grit-blasted screw-shaped implants with special emphasis on effects of blasting material and surface topography*. Biomaterials 1996;17:15-22.
52. Ericsson I, Johansson CB, Bystedt H, Norton MR. *A histomorphometric evaluation of bone-to-implant contact on machine-prepared and roughened titanium dental implants. A pilot study in the dog*. Clin. Oral. Impl. Res. 1994;5:202-206.
53. Ellingsen JE. *Bio-implant interface*. Boca Raton: CRC Press, 2003.
54. Ronold HJ, Ellingsen JE. *Effect of micro-roughness produced by TiO_2 blasting-tensile testing of bone attachment by using coin-shaped implants*. Biomaterials 2002;23:4211-4219.
55. Schwartz BZ, Raz P, Zhao G, Barak Y, Tauber M, Yao H, Boyan BD. *Effect of micrometer-scale roughness of the surface of Ti_6Al_4V pedicle screws in vitro and in vivo*. J. Bone. Joint. Surg. 2008;90:2485-2498.
56. Thor A, Rasmusson L, Wennerberg A, Thomsen P, Hirsch J, Nilsson B, Hong J. *The role of whole blood in thrombin generation in contact with various titanium surfaces*. Biomaterials 2007;28:966-974.
57. Mustafa K, Wennerberg A, Wroblewski J, Hultenby K, Lopez BS, Arvidson K. *Determining optimal surface roughness of TiO_2 blasted titanium implant material for attachment, proliferation and differentiation of cells derived from human mandibular alveolar bone*. Clin. Oral. Implants. Res. 2001;12:515-525.
58. Mustafa K, Wroblewski J, Hultenby K, Lopez BS, Arvidson K. *Effects of titanium surfaces blasted with TiO_2 particles on the initial attachment of cells derived from human*

mandibular bone. A scanning electron microscopic and histomorphometric analysis. Clin. Oral. Implants. Res. 2000;11:116-128.
59. Lossdörfer S, Schwartz Z, Wang L, Lohmann CH, Turner JD, Wieland M, Cochran DL, Boyan BD. *Microrough implant surface topographies increase osteogenesis by reducing osteoclast formation and activity*. J. Biomed. Mater. Res. A 2004;70A:361-369.
60. Stout KJ, Blunt L. *Nanometres to micrometres: three-dimensional surface measurement in bio-engineering*. Surf. Coat. Technol. 1995;71:69-81.
61. Chauvy PF, Madore C, Landolt D. *Variable length scale analysis of surface topography: Characterization of titanium surfaces for biomedical applications*. Surf. Coat. Technol. 1998;110:48-56.
62. Thomas TR, Rosen BG, Amini N. *Fractal characterisation of the anisotropy of rough surfaces*. Wear 1999;232:41-50.
63. Zinger O, Chauvy PF, Landolt D. *Scale-Resolved Electrochemical Surface Structuring of Titanium for Biological Applications*. J. Electrochem. Soc. 2003;150:B495-B503.
64. Buzio R, Malyska K, Rymuza Z, Boragno C, Biscarini F, De Mongeot FB, Valbusa U. *Experimental investigation of the contact mechanics of rough fractal surfaces*. IEEE T. Nanobiosci. 2004;3:27-31.
65. Brown CA, Charles PD, Johnsen WA, Chesters S. *Fractal analysis of topographic data by the patchwork method*. Wear 1993;161:61-67.
66. Wieland M, Textor M, Spencer ND, Brunette DM. *Wavelength-dependent roughness: A quantitative approach to characterizing the topography of rough titanium surfaces*. Int. J. Oral. Max. Impl. 2001;16:163-181.
67. Wieland M, Hanggi P, Hotz W, Textor M, Keller BA, Spencer ND. *Wavelength-dependent measurement and evaluation of surface topographies: application of a new concept of window roughness and surface transfer function*. Wear 2000;237:231-252.
68. MacDonald W, Campbell P, Fisher J, Wennerberg A. *Variation in surface texture measurements*. J. Biomed. Mater. Res., Part B 2004;70B:262-269.
69. Mattisson I, Ahlberg E. *Surface characterization and electrochemical properties of hierarchically structured titanium surfaces*. Accepted to Appl. Surf. Sci .
70. Davies JE. *Mechanisms of endosseous integration*. Int J Prosthodont 1998;11:391-401.
71. Hansson S. *Surface roughness parameters as predictors of anchorage strength in bone: a critical analysis*. J. Biomech. Eng. 2000;33:1297-1303.
72. Wennerberg A, Albrektsson T, Lausmaa J. *Torque and histomorphometric evaluation of c.p. titanium screws blasted with 25- and 75-mm-sized particles of Al_2O_3*. J. Biomed. Mater. Res. 1996;30:251-260.
73. Wennerberg A, Albrektsson T, Andersson B. *Bone tissue response to commercially pure titanium implants blasted with fine and coarse particles of aluminum oxide*. Int. J. Oral. Max. Impl. 1996;11:38-45.
74. Johansson C, Gretzer C, Jimbo R, Mattisson I, Ahlberg E. *Enhanced implant integration with hierarchically structured implants: A pilot study in rabbit*. Accepted to Clin Oral Impl Res .
75. Albrektsson T, Wennerberg A. *Oral implant surfaces: Part 1: Review focusing on topographic and chemical properties of different surfaces and in vivo responses to them*. Int. J. Prosthodont. 2004;17:536-543.
76. Williams DF. *On the mechanisms of biocompatibility*. Biomaterials 2008;29:2941-2953.
77. Raikar GN, Gregory JC, Ong JL, Lucas LC, Lemons JE, Kawahara D, Nakamura M. *Surface characterization of titanium implants*. J. Vac. Sci. Technol. A 1995;13:2633-2637.
78. Brunette DM, Tengvall P, Textor M, Thomsen P. *Titanium in medicine*. Berlin, Heidelberg, New York: Springer-Verlag, 2001.

79. Pan J, Liao H, Leygraf C, Thierry D, Li J. *Variation of oxide films on titanium induced by osteoblast-like cell culture and the influence of an H_2O_2 pretreatment*. J. Biomed. Mater. Res. 1998;40:244-256.
80. Sul Y, Johansson C, Byon E, Albrektsson T. *The bone response of oxidized bioactive and non-bioactive titanium implants*. Biomaterials 2005;26:6720-6730.
81. Ellingsen JE. *Pre-treatment of titanium implants with fluoride improves their retention in bone*. J. Mater. Sci.-Mater. M. 1995;6:749-753.
82. Isa Zakiah M, Schneider Galen B, Zaharias R, Seabold D, Stanford Clark M. *Effects of fluoride-modified titanium surfaces on osteoblast proliferation and gene expression*. Int. J. Oral. Max. Impl. 2006;21:203-211.
83. Maier J. *Physcial chemistry of ionic materials: Ions and electrons in solids*. Chichester, UK.: John Wiley & Sons Ltd., 2004.
84. Diebold U. *The surface science of titanium dioxide*. Surf. Sci. Reports 2003;48:53-229.
85. Roh B, Macdonald DD. *Effect of oxygen vacancies in anodic titanium oxide films on the kinetics of the oxygen electrode reaction*. Russ J Electrochem. 2007;43:125-135.
86. Blackwood DJ, Peter LM, Williams DE. *Stability and open circuit breakdown of the passive oxide film on titanium*. Electrochim. Acta 1988;33:1143-1149.
87. Tomkiewicz M. *The potential distribution at the titanium dioxide aqueous electrolyte interface*. J. Electrochem. Soc. 1979;126:1505-1510.
88. Johansson CB, Wennerberg A, Boström-Junemo K, Holmen A, Hansson S. *In vivo comparison of TiO_2 blasted- and fluoride modified implants in rabbit bone*. 7th World Biomaterials Congress, Sydney. 2004.
89. Ellingsen JE, Johansson CB, Wennerberg A, Holmen A. Improved retention and bone-to-implant contact with fluoride-modified titanium implants. Int J Oral Max Impl 2004;19:659-666.
90. Jackson DR, Omanovic S, Roscoe SG. *Electrochemical studies of the adsorption behavior of serum proteins on titanium*. Langmuir 2000;16:5449-5457.
91. Sul Y, Johansson CB, Roser K, Albrektsson T. *Qualitative and quantitative observations of bone tissue reactions to anodized implants*. Biomaterials 2002;23:1809-1817.
92. Huang YH, Xiropaidis AV, Sorensen RG, Albandar JM, Hall J, Wikesjo UME. *Bone formation at titanium porous oxide (TiUnite (TM)) oral implants in type IV bone*. Clin. Oral. Impl. Res. 2005;16:105-111.
93. Ivanoff CJ, Widmark G, Johansson C, Wennerberg A. *Histological evaluation of bone response to oxidized and turned titanium micro-implants in human jawbone*. Int. J. Oral. Max. Impl. 2003;18:15-22.
94. Chen ZX, Wang WX, Matsubara T, Ren LM. *Surface characteristics and in vitro biocompatibility of titanium anodized in a phosphoric acid solution at different voltages*. Biomed. Mater. 2009;4:1-8.
95. Das K, Bose S, Bandyopadhyay A. *Surface modifications and cell-materials interactions with anodized Ti*. Acta Biomaterialia 2007;3:573-585.
96. Santos E, Kuromoto NK, Soares GA. *Mechanical properties of titania films used as biomaterials*. Mater. Chem. Phys. 2007;102:92-97.
97. Delplancke JL, Winand R. *Galvanostatic anodization of titanium-I: Structures and composition of the anodic films*. Electrochim. Acta 1988;33:1539-1549.
98. Blackwood DJ, Peter LM. *The influence of growth rate on the properties of anodic oxide films on titanium*. Electrochim. Acta 1989;34:1505-1511.
99. Vanhumbeeck JF, Ryelandt L, Proost J. *On the relationship between local voltage maxima and efficiency changes during galvanostatic Ti anodising*. Electrochim. Acta 2009;54:3330-3338.

100. Proost J, Vanhumbeeck J-, Van Overmeere Q. *Instability of anodically formed TiO_2 layers (revisited)*. Electrochim. Acta 2009;55:350-357.
101. Hirschorn B, Orazem ME, Tribollet B, Vivier V. *Determination of effective capacitance and film thickness from constant-phase-element parameters*. Electrochim. Acta 2010;55:6218-6227.
102. Brug GJ, van der Eeden ALG, Sluyters-Rehbach M, Sluyters JH. *The analysis of electrode impedance complicated by the presence of a constant phase element*. J. Electroanal. Chem. 1984;176:275-295.
103. Ohtsuka T, Otsuki T. *The influence of the growth rate on the semiconductive properties of titanium anodic oxide films*. Corros. Sci. 1998;40:951-958.
104. Dolata M, Kedzierzawski P, Augustynski J. *Comparative impedance spectroscopy study of rutile and anatase TiO_2 film electrodes*. Electrochim. Acta 1996;41:1287-1293.
105. Kasemo B, Lausmaa J. *Metal selection and surface characteristics*. In: Brånemark P, A. ZG, Albrektsson B, editors. Tissue-Integrated Prostheses. Chicago: Quintessence Publishing Co., Inc., 1985. p. 99-116.
106. Sikora J, Sikora E, Macdonald DD. *The electronic structure of the passive film on tungsten*. Electrochim. Acta 2000;45:1875-1883.
107. Baumanis C, Bahnemann DW. *TiO_2 Thin film electrodes: correlation between photocatalytic activity and electrochemical properties*. J. Phys. Chem. C 2008;112:19097-19101.
108. Harrington SP, Devine TM. *Analysis of electrodes displaying frequency dispersion in Mott-Schottky tests*. J. Electrochem. Soc. 2008;155:C381-C386.
109. Munoz AG. *Semiconducting properties of self-organized TiO_2 nanotubes*. Electrochim. Acta 2007;52:4167-4176.
110. Radecka M, Rekas M, Trenczek-Zajac A, Zakrzewska K. *Importance of the band gap energy and flat band potential for application of modified TiO_2 photoanodes in water photolysis*. J. Power Sources 2008;181:46-55.
111. Anselme K. *Osteoblast adhesion to biomaterials*. Biomaterials 2000;21:667-681.
112. Chen X, Mao SS. *Titanium dioxide nanomaterials: synthesis, properties, modifications, and applications*. Chem. Rev. 2007;107:2891-2959.
113. Arnold M, Cavalcanti-Adam EA, Glass R, Blümme J, Eck W, Kantlehner M, Kessler H, Spatz JP. *Activation of integrin function by nanopatterned adhesive interfaces*. ChemPhysChem 2004;5:383-388.
114. Brammer KS, Oh S, Cobb CJ, Bjursten LM, vad der Heyde H, Jin S. *Improved bone-forming functionality on diameter-controlled TiO_2 nanotube surface*. Acta. Biomater. 2009;5:3215-3223.
115. Ohno T, Sarukawa K, Tokieda K, Matsumura M. *Morphology of a TiO_2 photocatalyst (Degussa, P-25) consisting of anatase and rutile crystalline phases*. J. Catal. 2001;203:82-86.
116. Chen LX, Rajh T, Wang Z, Thurnauer MC. *XAFS studies of surface structures of TiO_2 nanoparticles and photocatalytic reduction of metal ions*. J. Phys. Chem. B 1997;101:10688-10697.
117. Abayev I, Zaban A, Kytin WG, Danilin AA, Garcia-Belmonte G, Bisquert J. *Properties of the electronic density of states in TiO_2 nanoparticles surrounded with aqueous electrolyte*. J. Solid. State. Electrochem. 2007;11:647-653.
118. Ardizzone S, Cappelletti G, Minguzzi A, Rondinini S, Vertova A. *TiO_2 nanocrystal particles and electrodes. The combined role of pH and metal substrate*. J. Electroanal. Chem. 2008;621:185-197.
119. Berger T, Lana-Villarreal T, Monllor-Satoca D, Gómez R. *An Electrochemical Study on the Nature of Trap States in Nanocrystalline Rutile Thin Films*. J. Phys. Chem. C 2007;111:9936-9942.

120. Bohner M, Lemaitre J. *Can bioactivity be tested in vitro with SBF solution?* Biomaterials 2009;30:2175-2179.
121. Zyman ZZ, Rokhmistrov DV, Glushko VI. *Structural and compositional features of amorphous calcium phosphate at the early stage of precipitation*. J. Mater. Sci.- Mater. M. 2010;21:123-130.
122. Müller FA, Müller L, Caillard D, Conforto E. *Preferred growth orientation of biomimetic apatite crystals*. J. Cryst. Growth. 2007;304:464-471.
123. Wang CX, Wanga M, Zhoub X. *Nucleation and growth of apatite on chemically treated titanium alloy: an electrochemical impedance spectroscopy study*. Biomaterials 2003;24:3069-3077.
124. Ning CQ, Zhou Y. *In vitro bioactivity of a biocomposite fabricated from HA and Ti powders by powder metallurgy method*. Biomaterials 2002;23:2909-2915.
125. Barrere F, Snel MM, van Blitterswijk CA, de Groot K, Layrolle P. *Nano-scale study of the nucleation and growth of calcium phosphate coating on titanium implants*. Biomaterials 2004;25:2901-2910.
126. Sohmura T, Tamasaki H, Ohara T, Takahashi J. *Calcium-phosphate surface coating by casting to improve bioactivity of titanium*. J. Biomed. Mater. Res. 2001;58:478-485.
127. Uchida M, Kim HM, Kokubo T, Fujibayashi S, Nakamura T. *Effect of water treatment on the apatite-forming ability of NaOH-treated titanium metal*. J. Biomed. Mater. Res. 2002;63:522-530.
128. Di Virgilio AL, Reigosa M, Fernández M, de Mele L. *Response to UMR 106 cells exposed to titanium oxide and aluminum oxide nanoparticles*. J. Biomed. Mater. Res. A 2010;92:80-86.
129. Kranz I, Gonzalez JB, Dörfel I, Gemeinert M, Griepentrog M, Klaffke D, Knabe C. *Biological response to micron- and nanometer-sized particles known as potential wear products from artificial hip joints: Part II: Reaction of murine macrophages to corundum particles of different size distributions*. J. Biomed. Mater. Res. A 2009;89:390-401.
130. Huang HL, Chang YY, Lai MC, Lin CR, Lai CH, Shieh TM. *Antibacterial TaN-Ag coatings on titanium dental implants*. Surf. Coat. Tech. 2010;205:1636-1641.
131. Welch K, Cai Y, Engqvist H, Strømme M. *Dental adhesives with bioactive and on-demand bactericidal properties*. Dent Mater 2010;26:491-499.